

RIDGE WAVEGUIDE GaAs/Al_xGa_{1-x}As
MULTIPLE QUANTUM WELL LASER DIODES

A THESIS

SUBMITTED TO THE DEPARTMENT OF PHYSICS
AND THE INSTITUTE OF ENGINEERING AND SCIENCES
OF BILKENT UNIVERSITY

IN PARTIAL FULFILLMENT OF THE REQUIREMENTS
FOR THE DEGREE OF
MASTER OF SCIENCE

By

Abdullah Kâmuran Türkoğlu

February, 1994

TA

1300

787

1994

C.1

RIDGE WAVEGUIDE GaAs/Al_xGa_{1-x}As
MULTIPLE QUANTUM WELL LASER DIODES

A THESIS

SUBMITTED TO THE DEPARTMENT OF PHYSICS
AND THE INSTITUTE OF ENGINEERING AND SCIENCE
OF BİLKENT UNIVERSITY
IN PARTIAL FULFILLMENT OF THE REQUIREMENTS
FOR THE DEGREE OF
MASTER OF SCIENCE

By

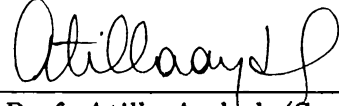
Abdullah Kâmuran Türkođlu

February, 1994

B023085

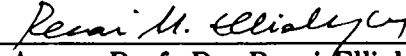
TA
1700
.T87
1994
C.1

I certify that I have read this thesis and that in my opinion it is fully adequate, in scope and in quality, as a thesis for the degree of Master of Science.



Prof. Atilla Aydın (Supervisor)

I certify that I have read this thesis and that in my opinion it is fully adequate, in scope and in quality, as a thesis for the degree of Master of Science.



Assoc. Prof. Dr. Recai Ellialtıođlu

I certify that I have read this thesis and that in my opinion it is fully adequate, in scope and in quality, as a thesis for the degree of Master of Science.



Prof. Cernaı Yalabık

Approved for the Institute of Engineering and Science:



Prof. Mehmet Baray,
Director of Institute of Engineering and Science

Abstract

RIDGE WAVEGUIDE GaAs/Al_xGa_{1-x}As MULTIPLE QUANTUM WELL LASER DIODES

Abdullah Kâmuran Türkoğlu

M. S. in Physics

Supervisor: Prof. Atilla Aydınlı

February, 1994

The study of solid-state laser structures in low dimensions has gained great deal of attention in recent years. The theory originated in early 1960s developed really fast along with new fabrication methods bringing geometries from macroscopic to sub-micron scale. This, in turn, made it possible to realize more complex semiconductor laser structures having multiple quantum wells in their active region with sub-milliampere threshold currents and tens of mWatt/facet optical light outputs. Today, after a long way of effort in the interest for MQW laser structures, quite challenging performances have been achieved.¹ However, due to complexity encountered during manufacturing and testing processes of these new lasing structures, it seems that overall technique still needs to be improved.

In this research conducted at BU Advanced Research Laboratories, design, fabrication and characterization of GaAs/Al_xGa_{1-x}As Multiple Quantum Well lasers is aimed. In the subsequent chapters, first the basic theoretical background for QW lasers is summarized, then the method followed during fabrication is reported, and finally, typical characteristics obtained after test studies are presented.

Keywords : *laser diode, multiple quantum well, ridge-waveguide, gallium arsenide, reactive ion etching.*

Özet

SIRT DALGAKILAVUZU GaAs/Al_xGa_{1-x}As ÇOKLU KUANTUM KUYU LAZER DİYODLAR

Abdullah Kâmuran Türkoğlu

Fizik Yüksek Lisans

Tez Yöneticisi: Prof. Atilla Aydınlı

Şubat, 1994

Düşük boyutlarda katıhal lazer yapıları üzerine yapılan çalışmalar son yıllarda büyük ilgi yaratmıştır. Altmışlı yıllarda ortaya atılan bu teori, yeni fabrikasyon metodlarıyla birlikte geometrileri makroskopik boyutlardan mikron-altı seviyelere indirgerken, oldukça çabuk gelişti. Bu şekilde, miliamper-altı eşik akım değerleri ve onlarca mW/yüz optik ışık çıkış güçlerine sahip, aktif bölgeleri çoklu kuantum kuyuları içeren, karmaşık yarı-iletken lazer yapılarının gerçekleştirilmesi sağlandı. Bugün, çoklu kuantum kuyu lazer yapılarıyla ilgili uzun süredir yapılmakta olan araştırmalarda oldukça üstün performanslara erişilmiştir.¹ Buna karşın, fabrikasyon safhalarının hassas ve karmaşıklığı işlem tekniklerinin hala geliştirilmeye ihtiyacı olduğunu ortaya koymaktadır.

BÜ İleri Araştırma Laboratuvarlarında gerçekleştirilen bu çalışmada, GaAs-Al_xGa_{1-x}As çoklu kuantum kuyu lazerlerinin tasarım, fabrikasyon ve karakterizasyonu amaçlanmaktadır. İleriki bölümlerde, ilkönce kuantum kuyu lazerlerine ait teorik temeller kısaca özetlenmekte, daha sonra fabrikasyonda izlenen metod anlatılmakta, ve son olarak da test çalışmaları sonrasında elde edilen karakteristikler sunulmaktadır.

Anahtar Kelimeler : *lazer diyod, çoklu kuantum kuyu, sırt-dalgakılavuzu, galyum arsenit, reaktif iyon aşındırma.*

Acknowledgement

First I would like to express my deep gratitude to my supervisor Prof. Atilla Aydınlı for his motivating suggestions and guidance throughout the development of this thesis. I am also grateful to Assoc. Prof. Dr. Recai Ellialtıođlu for his constructive remarks and comments during my study.

Here I wish to address my special thanks to my partner M. Koray Bozkurt for his sincere friendship and effective help in all stages of this study. I would also like to thank Murat Gre for providing a lot of support going far beyond technical matters.

I owe thanks to Dr. Feodor N.Timofeev for his invaluable encouragement and to all friendly people of Ioffe Institute, Russia, for accepting us to study in such a stimulating research environment they have created.

I would like to acknowledge Prof. J.Walter and Dr. F.Karouta from Eindhoven University of Technology, the Netherlands, for their valuable help, especially in providing laser structures.

Finally, I take this opportunity to thank all my friends in and out of Turkey for their patience and infinite morale support, particularly in times of despair and hardship.

This project was performed under the auspices of the Ministry of Defense, Undersecretariat for Defense Industries, Grant No: SSM-90-AG-033.50

Contents

Abstract	i
Özet	ii
Acknowledgement	iii
Contents	iv
List of Figures	vii
1 Introduction to Semiconductor Lasers	1
1.1 A Historical Perspective	1
1.2 Lasing Action in Semiconductors	2
1.3 Quantum Well Lasers	6
1.4 Theoretical Background for QW Lasers	8
1.4.1 Propagation and Gain	8
1.4.2 Optical Confinement Factor	10
1.4.3 Threshold Current Density	12
1.4.4 Near and Far Optical Field Distributions	14
1.4.5 Coupling between Quantum Wells	14

2	Fabrication	15
2.1	Process Steps	15
2.2	Samples	17
2.2.1	Wafer specification and cleavage	17
2.2.2	MQW Wafer Inspection	18
2.3	Cleaning and Surface Preparation	20
2.3.1	Sample Cleanup	20
2.4	Photolithography	21
2.4.1	An Overview of Photolithographic Process	21
2.4.2	Process Details	23
2.5	Etching (Dry)	26
2.5.1	Etching Techniques	26
2.5.2	LE-301 RIE System	28
2.5.3	Process Description	30
2.5.4	Etching Analysis	32
2.5.5	Cl ₂ Based Etching	36
2.5.6	RIE Induced Damage	37
2.6	Anodic Oxidation	39
2.7	Plasma Enhanced Chemical Vapour Deposition (PECVD)	41
2.8	Lift-Off	43
2.9	Metallization (<i>p</i> -contact)	44
2.10	Annealing (<i>p</i> -contact)	45
2.11	Thinning	45
2.12	Metallization (<i>n</i> -contact)	46
2.13	Annealing (<i>n</i> -contact)	47
2.14	Separation of Lasers	47

3	Test Results	49
3.1	Characterization	49
3.2	Definition of Basic Laser Parameters	50
3.3	Spontaneous Emission Spectra	51
3.4	Lasing Spectra	52
3.5	Current-Voltage Characteristics	53
3.6	Light-Output vs Current Characteristics	54
3.6.1	Threshold Current	55
3.6.2	Differential Quantum Efficiency	59
3.7	Field Distributions	62
3.7.1	Far Field Pattern	62
3.7.2	Near Field Pattern	65
4	Conclusions	67
	APPENDIX Properties of GaAs and $\text{Al}_x\text{Ga}_{1-x}\text{As}$	69
	Bibliography	70

List of Figures

1.1	Emission in a $p-n$ junction laser diode.	3
1.2	Energy band diagram of a $p - n$ junction laser diode	4
1.3	Band Gap and Refraction Index variation in $\text{Al}_x\text{Ga}_{1-x}\text{As}$	5
1.4	A simple Fabry-Perot Resonator model of Laser Diodes.	8
1.5	Power law GRIN profiles drawn for a MQW laser	10
1.6	Variation of Γ with respect to GRIN profile	11
1.7	Optical Radiation from a Ridge-Waveguide Laser.	14
2.1	Convention for identification of flats on wafers.	17
2.2	Layer Structure of the MQW samples	19
2.3	Photolithography using the negative and positive photoresist	22
2.4	Comparison of Wet and Dry etch profiles by SEM.	27
2.5	Basic schematics of Parallel-Plate LE-301 RIE system.	29
2.6	Dektak-Profile after etching	30
2.7	SEM-Profile after etching	31
2.8	Etch Rate Determination	32
2.9	Etching of GaAs, GaP and Si under CCl_2F_2 plasma	33
2.10	Oxygen and Freon-12 Plasma Comparison	34
2.11	$\text{Al}_x\text{Ga}_{1-x}\text{As}$ Etch Rate Data.	35
2.12	Chlorine based plasma results	36
2.13	Raman Scattering Spectrum of samples	37
2.14	Photoluminescence Spectrum of samples etched in Freon-12	39
2.15	Experimental Set-up for Anodic Oxidation	40
2.16	PECVD System Layout	42
2.17	Lift-Off Process	43

3.1	Spontaneous Emission Spectra	51
3.2	Lasing Spectra of 3QW Laser	52
3.3	I-V Characteristics of 3QW-B4 laser	53
3.4	I- P_{opt} Characteristics of 3QW and 4QW Lasers	54
3.5	Optical Power Output vs Forward Current Measurement System .	54
3.6	Cavity Length dependence of Threshold Current.	56
3.7	Plot of the Threshold Current Density versus Inverse Cavity Length.	57
3.8	Optical Power vs Current Characteristics of Sample-B8	59
3.9	Inverse Differential Quantum Efficiency vs Cavity Length	60
3.10	Experimental Set-up for Far-Field Measurements	62
3.11	Lateral and Transversal Far Field Pattern of 3QW Lasers	63
3.12	Lateral and Transversal Far Field Pattern of 4QW Lasers	64
3.13	Near-Field Radiation Pattern Measurement System	65
3.14	Lateral Near Field Pattern of 4QW-K10 Laser	66

Chapter 1

Introduction to Semiconductor Lasers

1.1 A Historical Perspective

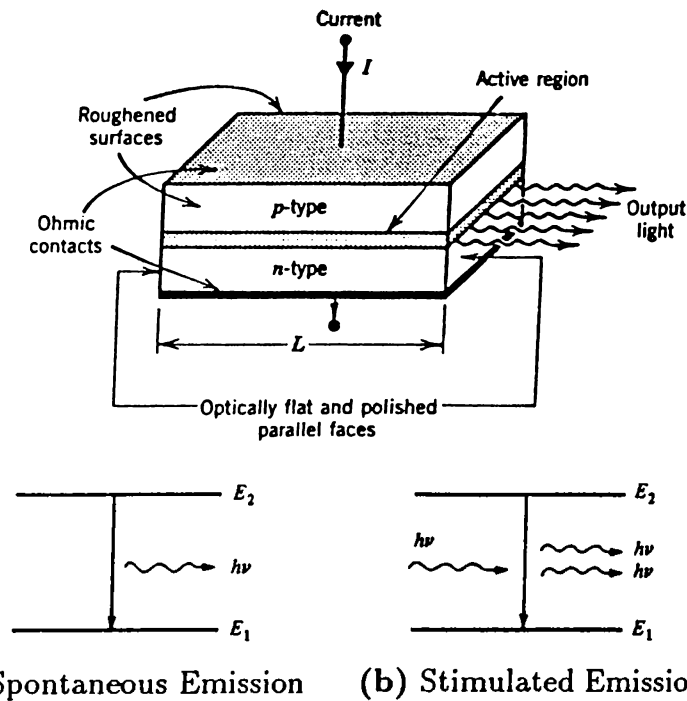
The search technology of lasing micro-structures began with observation of stimulated light emission in a forward-biased p - n junction by four independent groups simultaneously in 1962.²⁻⁵ This discovery of the laser diode triggered a great activity directed mainly toward finding new, reliable and powerful semiconductor structures. First breakthrough came with the development of ternary AlGaAs, leading Zh.I.Alferov, *et al.* from Ioffe Institute to demonstrate successful operation of first room-temperature semiconductor (GaAs/AlGaAs DH lasers grown by LPE) injection laser in 1970.⁶ Then the development of quaternary InGaAsP single crystal alloy followed, resulting first room-temperature long-wavelength LPE grown InP/InGaAsP lasers at 1.1 μm by J.Hsieh, *et al* at Lincoln Lab in 1976.⁷ Two years later, the operation of first room-temperature quantum well injection lasers having MOCVD grown GaAs/AlGaAs MQW structure was reported by two different research groups; N.Holonyak and D.Dupuis, *et al.*⁸ After three decades of effort, the laser diode has become a useful room-temperature device. And in the past few years, parallel to the advances in growth technology, great progress has been achieved in obtaining high-speed, low

threshold and high performance semiconductor lasers. Finally, the last milestone in the semiconductor laser field has been recorded in 1987. It was demonstration of first room-temperature heteroepitaxial CW GaAs/AlGaAs(MOCVD)-GaAs(MBE) laser operation shown by N.Holonyak (UIUC), Shichijo (TI) and Burnham (Xerox) separately.

The first visible laser diodes, based on InGaAlP materials, came on the market in 1988, extending potential uses of laser diodes to most of the mass applications in light-wave transmission previously addressed by He-Ne tubes. At 1.3-1.55 μm wavelengths, InGaAlP lasers provide the basis for long-distance fiberoptic communications. In general, laser diodes with wavelengths over 1 μm , regarded as long wavelength, are more suitable for optical communication. Those with wavelengths under 1 μm are particularly used in optical information for data storage and optical sensing purposes as in compact disc players ($\lambda = 780 \text{ nm}$), laser printers and barcode scanners ($650 \leq \lambda \leq 780 \text{ nm}$).

1.2 Lasing Action in Semiconductors

The word laser stands for light amplification by stimulated emission of radiation. Although, there exists a variety of semiconductor lasers differing in size, speed and power, essentially the same electronic action takes place in all of them. This lasing action can simply be analyzed by considering a basic semiconductor p - n junction. When an electron makes a downward transition from an upper to a lower energy level, an energy quantum is released in the form of light, *i.e* photon, as shown in a simple-two level band diagram of figure 1.1.a. This phenomena is said to be *spontaneous* in that each released photon acts independently. But if a monochromatic light source impinges upon the semiconductor, the electron in the upper energy level will act differently while the photon energy remains same as $E_2 - E_1$. Then, a photon is emitted as before while it drops to lower state, but now, its timing is such that it synchronizes with the incoming photons (Figure: 1.1.b). For this reason, radiation is said to be *coherent* since all the emitted photons are in phase with the photon that has



(a) Spontaneous Emission (b) Stimulated Emission

Figure 1.1: Emission in a p-n junction laser diode.

induced the transition. In fact, the presence of the external photons tends to increase the downward transition. Therefore, electrons are in this way *stimulated* to produce additional photons, resulting in optical gain or amplification.

To arrive at lasing action, there must be more electrons in upper state than in the lower state so that the number of stimulated emissions must be greater than that of the absorption transitions. So, a *population inversion* must exist in the system. However, this condition is not easily met in an ordinary p-n junction. Degenerately high doping at the p and n sides and also an extreme forward bias are needed to inject enough electrons and holes to put the quasi-Fermi levels at the band edges. High doping causes the band structure to be perturbed so as deep bandtails are formed which provides direct band-to-band transitions more likely to occur.²⁴ It is desired that carriers in semiconductor must exhibit high radiative transition probabilities which is only satisfied in direct[†] bandgap materials due to their energy-wave vector interrelation. Figure 1.2.a (from ref. 9) shows the band diagram of such a junction at thermodynamic equilibrium in which both

[†]Occasionally, the lasing action was observed in indirect band-gap materials, but that was achieved under very specific experimental conditions (Nahory *et al.*; Holonyak, Jr. *et al.*, 1971)

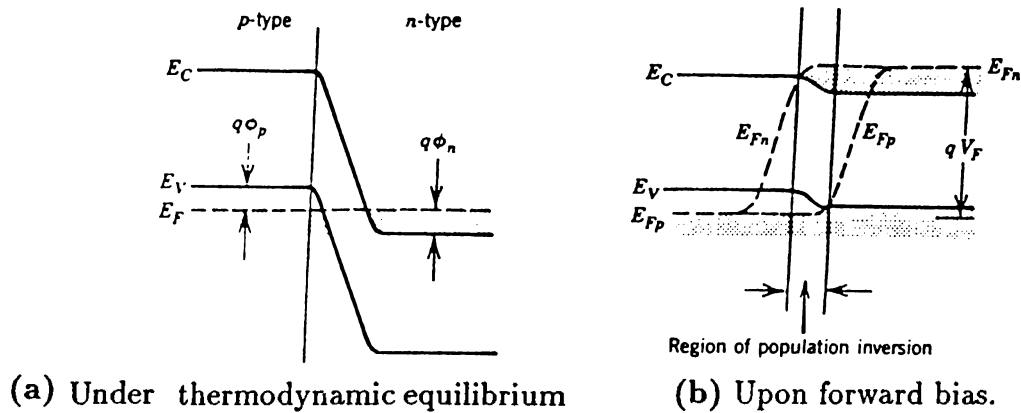


Figure 1.2: Energy band diagram of a $p - n$ junction laser diode

electrons and holes within each band are in thermodynamic equilibrium whereas no equilibrium exists between electrons and holes. Upon forward bias, electrons are injected from n-side into the p-side through transition region and recombine with holes radiatively while releasing photons of energy $h\nu$. (Fig. 1.2.b) Therefore, to achieve lasing, separation of quasi Fermi levels, $E_{fn} - E_{fp}$ must exceed the photon energy which is approximately equal to the bandgap, E_g . These photons are then kept in the transition region to provide subsequent stimulated emissions.

In the given $p-n$ junction model, however, there exist two problems. First, carriers injected to transition region diffuse away from the junction and this means a higher current is required to reach population inversion. Secondly, emitted light is excessively lost in the direction normal to the junction. One, therefore, needs an improved structure to concentrate injected carriers and emitted light near the junction's active region. Such confinement can be achieved by constructing a *double-heterojunction* where a p -GaAs is sandwiched between a p and n $\text{Al}_x\text{Ga}_{1-x}\text{As}$ layer. In such a heterostructure minority carriers cannot diffuse away from the narrow gap region because of the potential step in GaAs/AlGaAs interfaces. Since $\text{Al}_x\text{Ga}_{1-x}\text{As}$ has a wider bandgap than GaAs, a potential barrier is created which provides excellent carrier confinement.

The propagating optical field is also guided in p -GaAs active region

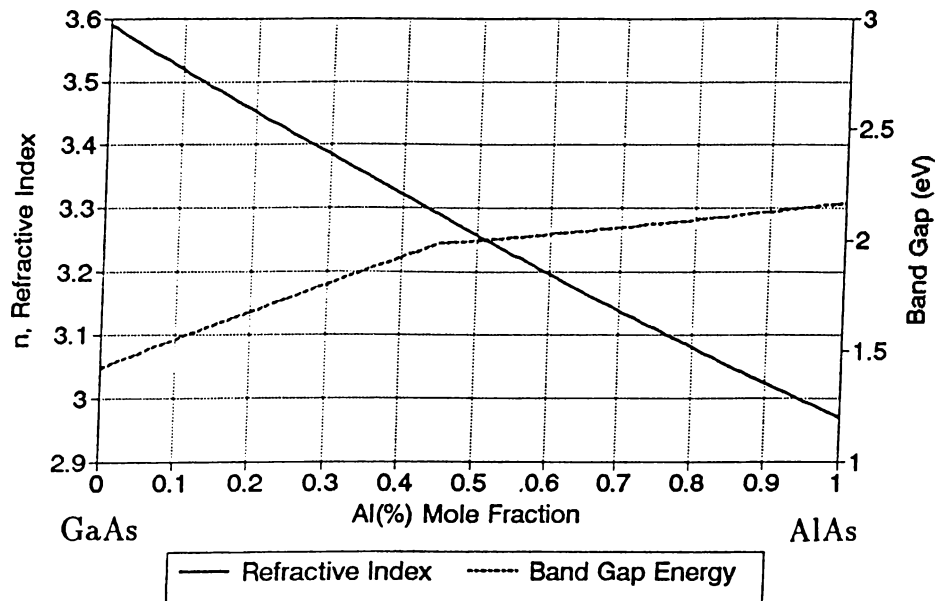


Figure 1.3: Band Gap and Refraction Index variation in $\text{Al}_x\text{Ga}_{1-x}\text{As}$.

automatically by the abrupt reduction of the refractive index outside the region. Since, as the Al content x of $\text{Al}_x\text{Ga}_{1-x}\text{As}$ is increased, its refractive index will decrease, the refractive index of the GaAs active layer is larger than the index of surrounding AlGaAs layers. In this way, the propagation of the electromagnetic radiation is optically confined within this slab waveguide geometry in the direction parallel to the layer interfaces. Refractive index and bandgap energy considerations of $\text{Al}_x\text{Ga}_{1-x}\text{As}$ are drawn in Figure 1.3.[†]

However, two other requirements are still needed in order to reach lasing threshold in a semiconductor laser diode; an optical cavity must be provided to build up the optical wave through positive feedback, and also the optical gain within the device must be greater than optical losses. This can be accomplished by using a resonant cavity consisting of two parallel mirrors, known as the *Fabry-Perot resonator*. This cavity is usually established by cleaving the GaAs crystal along the (110) planes. Then the cleaved surfaces will be perfectly parallel forming an ideal mirror. It is also possible to add dielectric coatings to these cleaved ends to control reflectivity and protect them from oxidation. The high reflectivity of a GaAs/air interface ($\sim 30\%$) gives optical feedback into the cavity

[†]A table related to physical properties of GaAs and $\text{Al}_x\text{Ga}_{1-x}\text{As}$ is given in appendix.

so that round-trip optical gain is achieved and, when it becomes sufficiently high to overcome the losses, the laser action results.

In the resonant emission only the longitudinal modes with a wavelength separation of $\lambda^2/2L$ are propagated.[‡] In fact, the light wave at this lasing mode can also resonate back and forth transversely, *i.e.* in the direction normal to the junction. The fundamental transverse mode is a sine-like standing wave with a half-length equal to the transverse cavity length.

1.3 Quantum Well Lasers

Optical radiation is guided by the slab waveguide geometry and amplified so that, above the onset of lasing, the optical output increases much more rapidly with drive current. It is usually the case that the thickness, d of the active (recombination) layer is less than the injected carrier diffusion length so that (if the heterobarsriers are sufficient to combine all the injected carriers) it is uniformly excited across its thickness. As d is reduced to less than $1\ \mu\text{m}$, only the fundamental optical mode can be guided and a fraction of this mode energy (Γ) is contained within the active layer, a consequence of Maxwell's equations applied to dielectric waveguides.¹¹

In this respect, quantum-well (shortly as QW) lasers with their ultrathin active layers are employed yielding several superior characteristics such as,

- Reduction in laser threshold current density, J_{th} ,¹²
- Reduced temperature dependence of J_{th} ,¹³
- Higher relaxation oscillation resonance frequency,
- Higher polarization stability,
- Higher differential gain with a narrow gain spectrum,¹⁴

[‡]Exact derivation is given in "Propagation and Gain" section.

In QW structures a series of energy levels and associated subbands are formed owing to the quantization of electrons in the direction of the quantum well thickness.¹⁶ This localization of carriers in ultrathin layers perpendicular to the layer plane is attributed to *quantum size effect*.¹⁷

The multiple quantum well structure which has a superlattice segment in its active region is achieved by modifying the core structure of QW lasers. Thus, upon bias, carriers are injected into the various GaAs wells that are separated by $\text{Al}_x\text{Ga}_{1-x}\text{As}$ barrier layers. By increasing the x content, *i.e.* increasing the depth of wells, density of states in the cavity can be increased. This increased density of states leads to a corresponding lowering of the threshold needed for achieving population inversion.¹⁸ By considering both the selection rule in the electron-hole recombination and of the energy separation between the heavy and light holes in the MQW structure, it is expected that the optical gain for a TE polarized wave would be much larger than that for a TM as shown experimentally by Okamoto.¹⁹ This can be stated as polarization-dependent optical gain.

Until 1981, MQW lasers studied were not containing higher than $x=0.3$ content in $\text{Al}_x\text{Ga}_{1-x}\text{As}$ barrier layers. It was Tsang¹⁸ who reported that using of larger AlAs composition in the cladding layers results in better optical confinement and also use of larger well-to-barrier ratio results in lower threshold.

By now, the idea of MQW has already been applied to its two- and three-dimensional conjugates *i.e.* quantum wire and quantum dots.

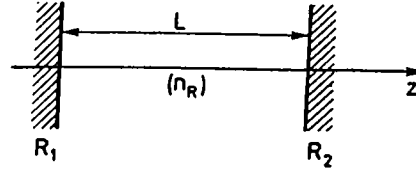


Figure 1.4: A simple Fabry-Perot Resonator model of Laser Diodes.

1.4 Theoretical Background for QW Lasers

1.4.1 Propagation and Gain

A common way for formulating basic gain equations in a laser diode is to construct the simple oscillator model of a Fabry-Perot resonator enclosed between two reflecting planes. As shown in Figure 1.4, resonator employs two confronting mirrors with reflection coefficients R_1 and R_2 where the space between filled with a light amplifying material of refractive coefficient, n_R . There are three kinds of modes describing the oscillations of the electromagnetic field in this 3D rectangular resonator. The wavelength of radiation concentrated in these modes can be found from the standing wave condition inside the active layer:

$$\left(\frac{q\pi}{d_r}\right)^2 + \left(\frac{s\pi}{W_r}\right)^2 + \left(\frac{m\pi}{L}\right)^2 = \left(\frac{2\pi n_R}{\lambda}\right)^2; q, s = 0, 1, 2, \dots, m = 1, 2, 3, \dots \quad (1.1)$$

where d_r , W_r and L denotes respectively the thickness, width and the length of the resonator. The indices m , s and q are then the numbers that characterizes the type of the mode; longitudinal, lateral or transversal. If we assume only longitudinal modes are propagating ($q=s=0$), then above equation reduces to,

$$m \frac{\lambda/2}{n_R} = L \quad (1.2)$$

here $m=1,2,3,\dots$ corresponds to order of longitudinal modes propagating inside the laser. It follows from equation 1.2 that the phase condition for the resonance oscillations to occur is satisfied when there exist an integral number of half-wavelengths between the end mirrors. Differentiating this equation with respect to λ and substituting the value of m from above, give the separation between the

adjacent longitudinal modes,

$$d\lambda = \frac{\lambda}{2n_R L [1 - (\lambda/n_R)(dn_R/d\lambda)]} \quad (1.3)$$

Then the spacings between successive longitudinal modes on the spectral characteristic can be found as,

$$\Delta\lambda = \frac{\lambda^2}{2L(n_R - \lambda dn_R/d\lambda)} = \frac{\lambda^2}{2Ln_G} \quad (1.4)$$

where n_G is the group index of refraction.

In the given resonator model, the plane wave propagating in z direction can be expressed using the condition of equation 1.2 as,

$$E_i \exp\left[\frac{i \cdot 2\pi n_R z}{\lambda}\right] \cdot \exp[(g - \alpha_i)z] \quad (1.5)$$

where λ is free-space wavelength, g is gain and α_i is the coefficient of internal losses. For a standing-wave oscillation to occur, the wave amplitude after a round-trip should be equal to its amplitude, which can be interpreted as,

$$R_1 R_2 \exp\left[\frac{i \cdot 4\pi n_R L}{\lambda}\right] \cdot \exp[(g - \alpha_i)2L] = 1 \quad (1.6)$$

Hence the amplitude condition for the oscillations to occur is,

$$R_1 R_2 \exp[(g - \alpha_i)2L] = 1 \quad (1.7)$$

and from here threshold gain can be written as,

$$g_{th} = \alpha_i + \frac{1}{2L} \ln \frac{1}{R_1 R_2} \quad (1.8)$$

The reflection coefficient at the semiconductor/air boundary is generally defined as $R = \left(\frac{n_R - 1}{n_R + 1}\right)^2$. If the reflection coefficients of the two resonator mirrors are made equal to the reflection coefficient at this boundary ($R_1 = R_2 = R$)[†] then the threshold gain given by equation 1.8 can be put in the form of

$$g_{th} = \alpha_i + \frac{1}{L} \ln \frac{1}{R} = \alpha_i + \alpha_{end} \quad (1.9)$$

in which the end losses, α_{end} term stand for side-mirror losses.

[†]Calculation of reflection coefficients for varying thickness of active layer is discussed by Ikegami.²⁰

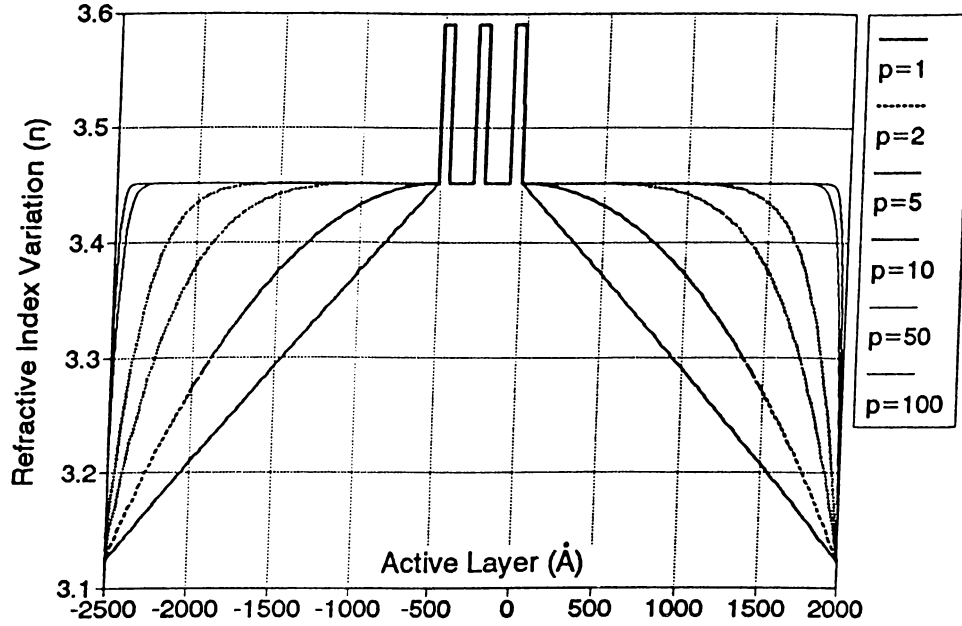


Figure 1.5: Power law GRIN profiles drawn for a MQW laser

1.4.2 Optical Confinement Factor

The efficiency of electromagnetic field confinement in the active layer is described by confinement factor, Γ , which is defined as the ratio of energy flux confined within the active layer to the total energy flux of the radiation generated in the laser. Confinement factor is strongly dependent on the geometry of optical cavity and refractive index variation inside. Basically, it can be defined by an equation of the form,

$$\Gamma = \frac{\int_{-d/2}^{d/2} |\mathcal{E}_i|^2 dx}{\int_{-\infty}^{\infty} |\mathcal{E}_i|^2 dx} \quad (1.10)$$

Until it is first proposed by W.Tsang,¹⁵ heterostructure lasers were limited to well designs with abrupt step index change at the boundaries. He reported graded index separate confinement heterostructure (GRIN-SCH) profile while achieving separate carrier and optical confinement in parabolically graded-index waveguide. Various index profiles can be described using the so-called power law index changes;

$$n(r) = n_w \left(1 - 2\Delta \left(\frac{2r}{w}\right)^p\right)^{1/2}, |r| \leq w/2 \quad (1.11)$$

where w is the total width of the active layer, r is the distance from the center of the waveguide, p is the exponent of the power law, $\Delta = (n_w - n_c)/n_w$ with

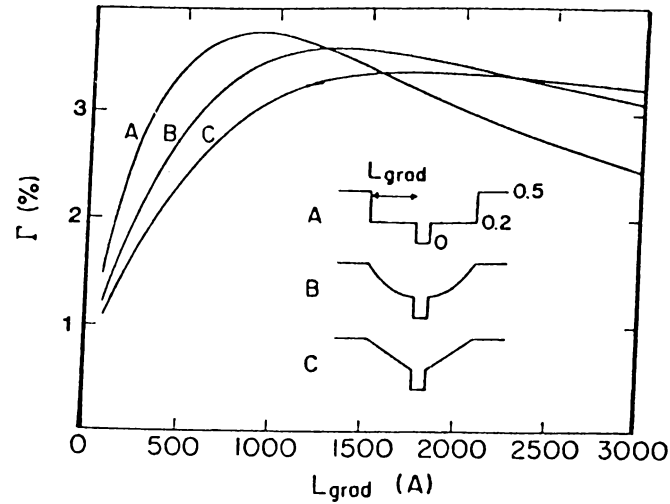


Figure 1.6: Variation of Γ with respect to GRIN profile

n_w , n_c are the refractive indexes at the well and cladding layers respectively. In figure 1.5 resulting index profile is drawn for $w=4000 \text{ \AA}$, $n_w = 3.4516$ for $x=0.2$ and $n_c = 3.1376$ for $x=0.7$ in $\text{Al}_x\text{Ga}_{1-x}\text{As}$. Notice that in the limit of very large p (~ 100), profile approaches that of the regular SCH.

McIlroy, *et al*²¹ calculated the values of Γ for varying guiding layer thicknesses of three main index profiles. The variation of Γ with power, p changing from infinity to unity ($A : p \sim \infty, B : p \sim 2, C : p \sim 1$) is given in figure 1.6 for a well width of 100 \AA . It is worth noting here that the linearly graded profile when p is equal to unity also describes the profile and confinement behaviour of the structures used in this study.

Figure 1.6 also indicates the difference in confinement behaviour between a separate confinement heterostructure (SCH) and normal abrupt junction heterostructure lasers. Confinement factor, Γ decreases rapidly when the guiding layer thickness is made less than 500 \AA where the total active layer thickness start to become comparable with the wavelength of the radiation in the semiconductor.²³ This means that any increase to be made in the quantum well width will highly effect the optical confinement in this regime. Therefore in abrupt junction heterostructure lasers optical confinement is strictly dependent

on quantum well width(s). However, SCH lasers are generally designed so that the guiding layer thicknesses are made larger than $0.1 \mu\text{m}$, thus the degree of optical confinement is mainly determined by the geometry of the guiding layers as shown in the figure. If we name total confinement factor as Γ_{net} and define,

$$\Gamma_{net} = \Gamma_{conf} + \Gamma_{well} \quad (1.12)$$

where Γ_{conf} refers to confinement in the guiding layers confining core well arrangement and Γ_{well} is the contribution by quantum well(s) to the Γ_{net} , then in the cases where guiding layer thickness is larger than $0.1 \mu\text{m}$ the Γ_{conf} term becomes dominant and the second term can be neglected. Therefore if we have a core MQW arrangement at the same time, then the net confinement factor is independent of the number of wells.²²

1.4.3 Threshold Current Density

The gain, g in equation 1.5 is referred as material gain. If it is uniformly distributed across the active region ($g(x) = g$), then the modal gain, \mathcal{G} , confined within active region can be expressed as

$$\mathcal{G} = \Gamma g \quad (1.13)$$

by using confinement factor Γ . To achieve at lasing for the fundamental transverse mode to be excited, the following threshold condition should be satisfied,²³

$$\mathcal{G}_o = \Gamma_o g \geq \Gamma g_{th} = \alpha_i + \alpha_{end} \quad (1.14)$$

where g_{th} denotes threshold local gain, α_{end} is the second term in equation 1.9 corresponding to end losses and α_i is the internal losses which is given by the sum,

$$\alpha_i = \Gamma_o \alpha_{fc} + (1 - \Gamma_o) \alpha_{out} + \alpha_s + \alpha_c \quad (1.15)$$

Here, α_s and α_c , α_{fc}^\dagger and α_{out} are the coefficients representing optical scattering losses in the active region and in the cladding layers, free-carrier absorption in

[†]The free carrier absorption coefficient for GaAs²⁴ at room temperature may be written as $\alpha_{fc} = 3 \times 10^{-18}n + 7 \times 10^{-18}p, \text{ cm}^{-1}$.

active layer and in the cladding layers, respectively. Therefore, in practice it is quite difficult to separate the different contributions to α_i .

The equation for the threshold current density J_{th} of (AlGa)As broad-area Fabry-Perot double heterostructure (DH) lasers is given by ,

$$J_{th} = \frac{d}{\eta_i} \left[J_o + \frac{1}{\Gamma a} (\Gamma \alpha_{fc} + (1 - \Gamma) \alpha_{out} + \alpha_s + \alpha_c + \alpha_{end}) \right] + j_N + j_P \quad (1.16)$$

where j_N and j_P are densities of electron and hole leakage currents, and a is given as $5 \times 10^{-2} \text{ cm}\mu\text{m}/\text{\AA}$.²⁴ Coupling loss, α_c , may be assumed negligible if cladding layers are thick ($\sim 0.2 \mu\text{m}$) and α_{out} can be taken as $\sim 10 \text{ cm}^{-1}$. Thus, α_i is typically found around $10\text{--}20 \text{ cm}^{-1}$. The equation given in 1.16 can be written more specifically using α_i as,

$$J_{th} = \frac{J_o d}{\eta_i} + \frac{d}{\eta_i \beta \Gamma} \alpha_i + \frac{d}{\eta_i \beta \Gamma} \frac{1}{L} \ln \frac{1}{L} \quad (1.17)$$

with the gain-current relation assuming the linear form,

$$g_{max} = \beta (J_{nom} - J_o). \quad (1.18)$$

In 1.17, we can call the first term as intrinsic term, the second as internal loss term and the last one as mirror loss term. Here it is seen that main contribution to J_{th} comes from the first intrinsic linear term if active layer is not much less than 1000 \AA .²⁵ For the case where $d \sim 700 \text{ \AA}$, mirror and internal loss term start to become effective due to decreased optical confinement factor Γ . The term J_{nom} in equation 1.18 is called as nominal current density which is related to actual current density J as $J_{nom} = \eta_i (J/d)$.²⁶

Using the multiple quantum well structure as an active region, several research groups have demonstrated room-temperature continuous-wave operation of lasers with very low threshold currents in the range $0.88\text{--}1.0 \text{ mA}$ to date.^{27,28} Uncoated MQW stripe-geometry lasers with thresholds as low as $1.0\text{--}1.6 \text{ mA}$ have also been achieved by growth on ridge-structure.²⁹ The progress has been made, in large part, by the optimization in MQW design and device structure.³⁰

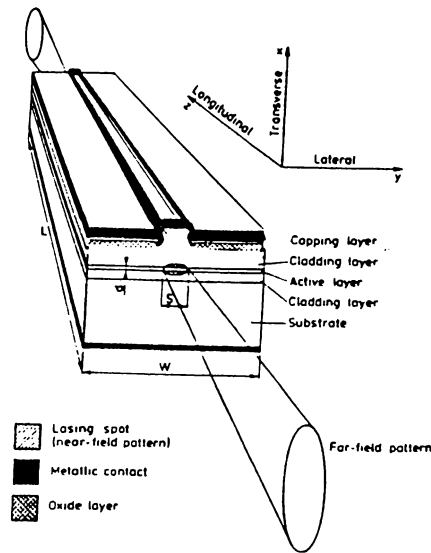


Figure 1.7: Optical Radiation from a Ridge-Waveguide Laser.

1.4.4 Near and Far Optical Field Distributions

Active layer structure is rectangular rather than cylindrically symmetric.(Fig. 1.7) Emitted beam from the active layer is refracted and takes the form of a vertical ellipse (far-field pattern), whereas it has the shape of a horizontal ellipse (near-field pattern) on the surface of the mirrors. Therefore, a diode with an acceptable light output has two beam-divergence angles. The ratio between that two angles taken perpendicular and lateral with respect to geometry is called as aspect ratio which is given by $\frac{\theta_{\perp}}{\theta_{\parallel}}$. In general, the nearer this ratio is to unity the better, then the beam is more circular.

1.4.5 Coupling between Quantum Wells

In addition to optical absorption and stimulated emission, quantum states of electrons and holes is also observed to couple via tunneling for a quantum well of GaAs bounded by thin $\text{Al}_x\text{Ga}_{1-x}\text{As}$ barriers.³¹ This coupling of quantum wells is due to overlapping phenomena in so-called *communicating* wells adjacent to each other. This may lead to a series effect in multiple quantum wells thereby increasing the threshold current density.¹⁸ However, the 150 Å barrier thickness of the laser used in this study prevents quantum wells from coupling as also verified by Dingle, *et al.*³²

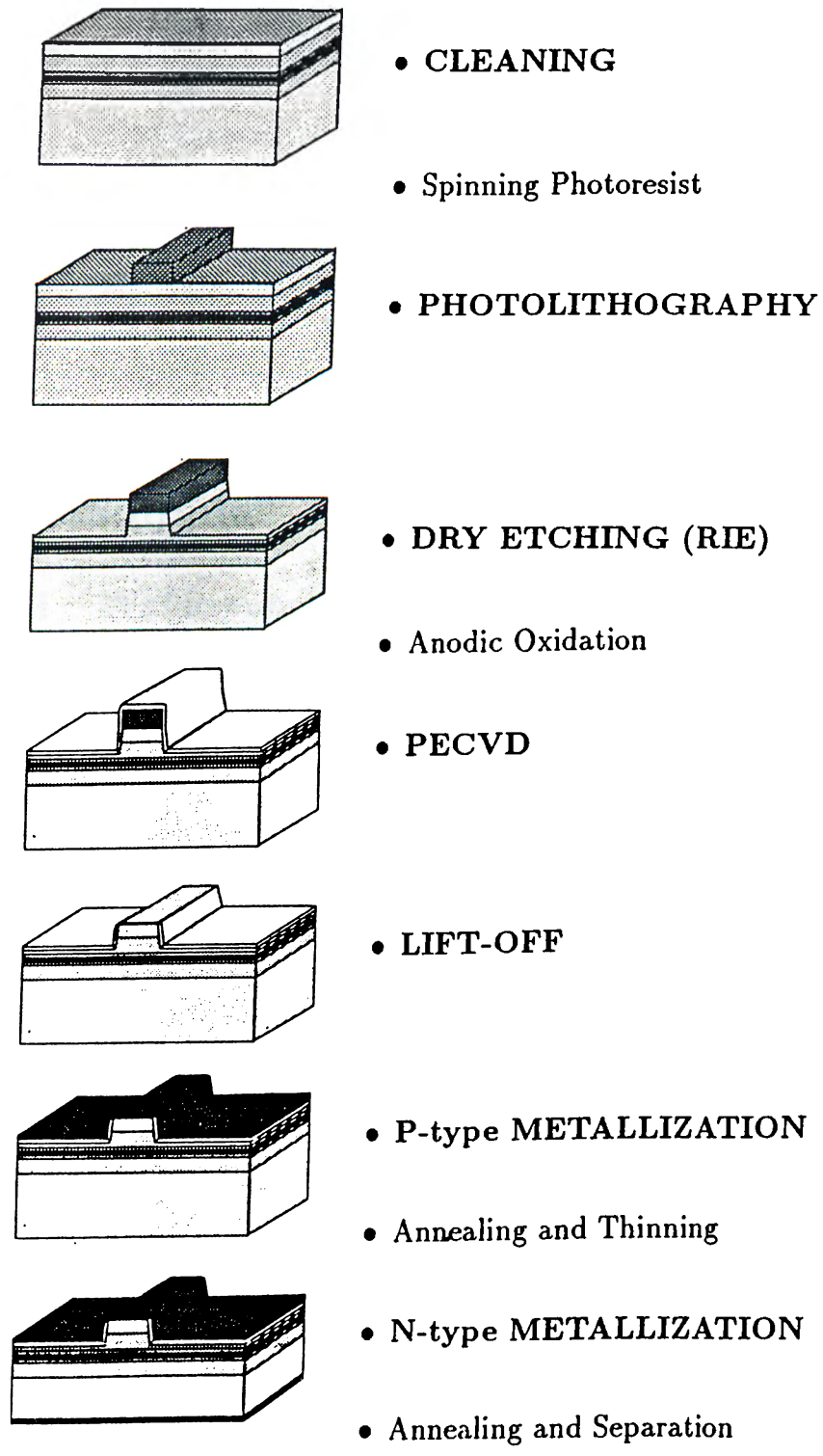
Chapter 2

Fabrication

2.1 Process Steps

The fabrication of laser diode involves many steps, each of which must be optimized to achieve acceptable performance with reliable and repeatable manufacturing yields. (Table:1) Subsequent sections of this chapter are concerned with specific stages followed in the fabrication of a ridge-stripe type MQW laser diode. At the beginning of each section, an overall view of that processing step is given. Then experimental set-up and parameters chosen are described. Finally, a respective discussion related to processing method is included at the end.

Table:1 Laser Diode Processing Flow Chart



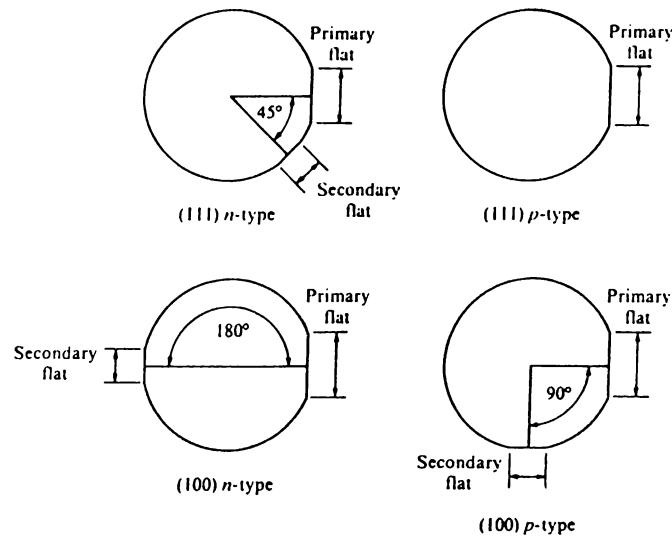


Figure 2.1: Convention for identification of flats on wafers.

2.2 Samples

2.2.1 Wafer specification and cleavage

The laser diode fabrication typically begins with the form of a circular GaAs "wafer" 2 to 4 inch in diameter and approximately 0.5 mm thick. These wafers are readily provided with the cited surface orientations, thereafter epitaxial layer arrangement (for example a MQW structure) is grown on the GaAs substrate. Since it would be difficult to process the whole wafer, and also a complete waste to spend it in a single process run, it was preferred to *cleave* wafers to separate into appropriate pieces. To do that, a short groove was opened on the front surface by precisely drawing a diamond-tipped scribing tool along the desired breakage line at the primary flat edge of the wafer. Primary flat is the long straight-line region along the periphery of the wafer and positioned originally to identify crystalline directions lying within the surface plane. The relative orientations of the primary and secondary flats indicate both the wafer type (n or p) and surface orientation as shown in Figure 2.1.³³ For (100) oriented wafers of our interest, the primary flat along the edge of the wafer is a (011) plane, and the normal to this flat is defined by [011] direction.

Then, to break the wafer, a small stress (to avoid damaging the structure) is applied on one side of the scribe line and wafer is bent to cut into two pieces. However, since GaAs is very brittle and has a tendency to break easily in arbitrary directions if not cleaved in the proper direction, a knowledge and understanding of the wafer surface orientation and respective indices are essential for a successful breakage. This idea based on the fact that crystal GaAs wafer, when mechanically stressed at room temperature, is cleaved most readily on the (110) planes.³⁴ This feature completely comes from the nature of GaAs crystal structure. It is, basically, a result of variation in atomic packing density for different planes in which packing density and available bonds decrease as we go from (111) to (100) to (110). Therefore samples with perfect rectangular geometry are obtained by cleaving (100) oriented GaAs wafers perpendicular to the major axis, in the [011] direction.

2.2.2 MQW Wafer Inspection

Process samples consisted of pieces of having approximately 2 cm² area obtained by cleaving nominally around 400 μm thick (100) oriented 3" (80 mm in diameter) GaAs MQW-wafers. These molecular beam epitaxy (MBE) grown MQW wafers were supplied by University of Eindhoven, the Netherlands. The device structure of the GaAs/AlGaAs MQW laser diodes used for this research is given in figure 2.2. The micrograph taken by JSM-6400 SEM shows that the interfaces are sharp and the layers are uniform. In the figure, aluminum contents and thicknesses around the active layer are also indicated.

The structure is grown by MBE on an *n*-doped (100) GaAs substrate starting with a substrate temperature of 580 °C and reaching up to 800 °C when growing Al_{0.7}Ga_{0.3}As cladding layers. The core active layer consist of a quantum well arrangement of three or four 70 Å thick undoped GaAs quantum wells separated by 150 Å thick Al_{0.2}Ga_{0.8}As barriers, which is centered between two 0.2 μm thick Al_{*x*}Ga_{1-*x*}As optical guiding layers having linearly graded Al profile(*x*:0.2→0.7). This is then sandwiched between Be-doped *p* and Si-doped *n*-type Al_{0.7}Ga_{0.3}As

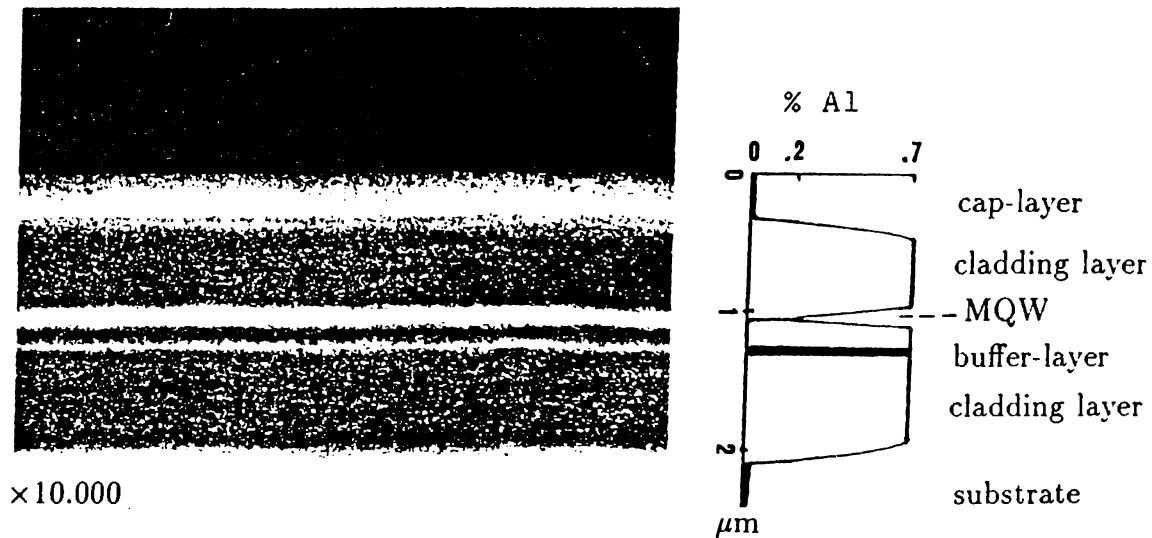


Figure 2.2: Layer Structure of the MQW samples

outer-cladding layers. The aluminum fraction in the cladding layers is taken as 0.7 so that the light and carrier confinement are sufficiently high. The thickness of these cladding layers are around $1 \mu\text{m}$ for p - and $1.25 \mu\text{m}$ for $n\text{-Al}_{0.7}\text{Ga}_{0.3}\text{As}$ layer to ensure low waveguide losses.

As seen in the cross-sectional figure, n -type cladding layer incorporates a Si doped 500 \AA thick superlattice buffer-layer $0.25 \mu\text{m}$ beyond the active layer, which is made up of repetition of ten period $25 \text{ \AA} \text{ Al}_{0.7}\text{Ga}_{0.3}\text{As}/25 \text{ \AA} \text{ GaAs}$ layers. The 0.7 aluminum content of cladding layers decreased down to zero in $0.3 \mu\text{m}$ distance away from both sides. Finally, layer arrangement is terminated by growing a $0.75 \mu\text{m}$ $p\text{-GaAs}$ capping layer at a substrate temperature of $500 \text{ }^\circ\text{C}$ for the p -type contact. The doping density of the top cap-layer is kept high at about 3.56×10^{19} for the nonalloyed electrode consisting of Ti/Pt/Au to form a good ohmic contact.

2.3 Cleaning and Surface Preparation

2.3.1 Sample Cleanup

To prepare samples for the application of photoresist, a sequential multistep rinsing treatment has been applied, the front and back sides of the wafer is cleaned chemically and mechanically. First, samples were immersed in hot TriChloroEthane (TCA) bath for 2–3 minutes. One method applied to ensure TCA cleanup has been made thoroughly was holding sample just above the solution to the TCA vapors and to check if it evaporates uniformly from the surface. This is a particularly clean method as only distilled vapors act on the sample.

Secondly, a hot bath of acetone[†] was applied for two minute duration. During acetone bath, it seemed that cleaning the sample surface using a clean cotton tipped tool worked quite well to clean out all residual materials. This method can be stated as a mechanical brushing technique and has been proved to be very effective in removing particle contaminants by overcoming the adhesion forces.⁴⁰ But, for the very dirty samples (re-used ones) two-bath immersion treatment of first acetone bath for 5 min and 2 to 3 min in a second was preferred. In the third step, dipping for one minute in cold Isopropanol followed. At this stage, it is also possible to apply a 18 M Ω -cm deionized (DI) water spray rinse where this step was skipped in some process runs. Finally, samples were dried under continuous Nitrogen(N₂) gas flow. Thus a clean and dry surface is provided to ensure good photoresist adhesion in the next step.

One can also make sure that all the chemicals (that might have penetrated into sample during cleaning) are evaporated by putting the samples into an oven for 1–2 minutes at about 80–90 °C afterwards. This can be termed as *dehydration baking* and helps to improve adhesion of resist by creating more mechanical-chemical bondings on the surface.

The only precaution must be taken in following this procedure is that one should not allow the wafer to become dry before going to subsequent rinsing, as

[†]Boiling point of acetone is 56.2 °C.

the evaporation of one of the solvents would leave behind residues that may not be soluble in the solvent used in the next step.

It is known that when a clean GaAs wafer is left open to air, an oxide layer as thick as 30 Å grows in four days.³⁵ Moreover, a carbon overlayer is then formed when the steady-state thickness is reached. This thin oxide-carbon layer at the interface, highly affect the contact performance especially in metallization giving a poor contact quality and failure in reproducibility.³⁶

2.4 Photolithography

2.4.1 An Overview of Photolithographic Process

Photolithography is the name given to complete process of replicating the mask pattern on the wafer surface using photoresist as the masking element. Photoresist, shortly as PR, is basically a photosensitive polymeric material commonly supplied in liquid form. This process starts with deposition of a thin photoresist layer over wafer surface by spin coating. To do that, the wafer is held on a vacuum chuck and drops of liquid photoresist is dispensed onto wafer surface. While resist is laying down, the spinner is spun at high speed to produce a uniform resist film across the surface by means of centrifugal forces spreading resist outwards.

The thickness of the resist coated, depends on its viscosity and is inversely proportional to the square root of the spinning speed.³⁷ Therefore, spinner is rotated accurately at a predetermined speed for a specified time. Spin time is adjusted to match the duration in which PR thickness is stabilized. Resist must be deposited thick enough (at least 0.3–0.4 μm) so that it can withstand etching to avoid resist erosion. This sets a lower limit on photoresist film thickness.

Next, a drying step referred as *soft baking* or *prebaking* is applied by simply heating the PR coated wafer in the oven in air atmosphere. Softbaking is primarily used to harden the resist by removing the solvent and water remaining

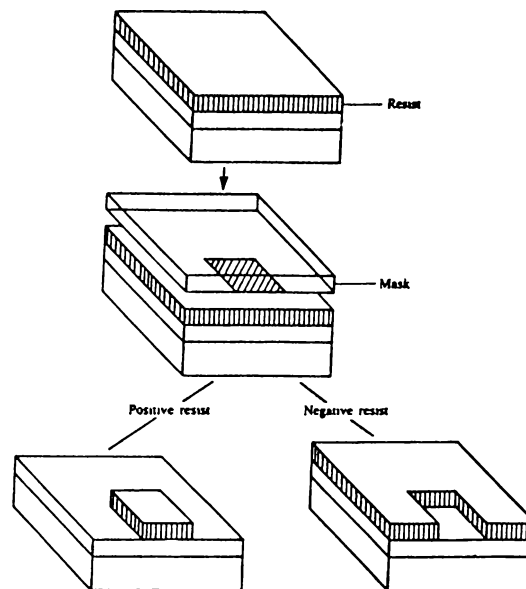


Figure 2.3: Photolithography using the negative and positive photoresist

in the film after spin-on. This removal, while improving adhesion, decreases the resist thickness.³⁸ After that, mask alignment and exposure step is carried out. Mask is a few mm thick, square glass plate with one of its faces containing the ridge-pattern to be generated on wafer surface.

Using mask aligner, wafers were placed under mask onto an adjustable xy stage for alignment. In separation mode, the wafer is carefully positioned within a few micrometers of the mask. After alignment, the face of the mask covered with pattern is brought into direct contact with the wafer, in the contact printing mode. But here, closeness of the mask and wafer may cause damage and contamination of the mask. Following alignment, the photoresist is exposed through the mask with high-intensity ultraviolet light from a mercury lamp.

In subsequent developing stage, the exposed areas of the resist is removed chemically in diluted developer solution. Photoresist acting in this manner is called as positive resist and a copy of the same mask pattern remains on wafer surface.(Fig. 2.3) Negative resists, on the other hand, acts oppositely and negative image results after washing away the irradiated or shadowed regions. DeForest³⁹ discusses origin of this feature related to exposure mechanism and chemical reactions, postulated first by Sus and Levine in 1944.

After exposure and before development, a second bake referred as *postbake* (sometimes it is made after development and this time called as *hardbake*) is also possible to add advantages of hardening resist, increased contrast and better adhesion. Postbaking increases the resistance of the resist to the etching process, because hardened resist is rather difficult to remove as solvent penetration becomes restricted. However, this may cause problems in lift-off applications and therefore not preferred.

2.4.2 Process Details

The masking material used is 0.1 μm prefiltered AZ-5214E (American Hoechst) positive photoresist. This is one of the new resists whose spectral absorption peak is at about 360 nm, so it is ideally matched for mercury i-line (365 nm) photolithography.

Resist film with a thickness of approximately 1 μm were obtained by spinning at 5000 rpm for 30 seconds. Just prior to application of resist 100% HMDS (hexamethyldisilazene) were applied to cover the wafer so that it promotes the adhesion of resist to wafer. While doing that, HMDS was left 5–15 sec before spinning, depending on the level of adhesion needed. After PR dispense, it was seen that some increase in PR thickness inevitably occurs at the edges of the wafer probably due to surface tension of the liquid. However, these regions helps a lot in determining the exact distance where this regions comes into contact first with mask in alignment.

Following the resist application samples are soft-baked at 90 °C for 40 minutes. Since the degree of solvent removal, temperature and time of the softbake directly impact on exposure parameters, these are critical parameters requiring optimization first. In this respect, it was seen that between 90 and 100 °C is an ideal range for temperature, and by achieving 100 °C, photoresist starts to reduce its apparent sensitivity as indicated by Elliott.⁴⁰ This degree is optimized for softbake time changing between 30–40 min.

Mask alignment and exposition steps were carried out by following conventional photolithography techniques in Karl-Suss MJB-3 Mask Aligner. The

mask used was comprising parallel, 5 and 12 μm wide[†] dark lines (stripes) on a clear background for positive photoresist application. In exposition, aligner was brought to soft contact printing mode whereby a reduced vacuum is applied to prevent the extreme pressure between mask and resist. Then, sample is aligned under mask so that stripes will be parallel to major axis of the wafer to simplify cleaving and separating procedure in the final step.

Samples were then exposed to define ridges on the sample surface under 12 mW-UV for about 38 seconds. For 12 mW exposition, it was observed that resist is underexposed if exposition time is decreased under 33 sec and there exists a tendency for the pattern formation to be incomplete. On the other hand, overexposure occurred with extreme loss of pattern if this interval is increased to a value as high as 44 sec. This behaviour can be attributed to penetration of excessive scattered light under the mask edges by the time and exposition of the region not directly irradiated by the light source.

Developing step is completed in one minute in AZ-400K Developer/DI water bath(1:4). Resist dissolution rate in developer is found to be strongly dependent on developer dilution ratio and softbaking parameters. If developer concentration is increased, for example to 1:3, developing time is observed to reduce as well, but leaving a more distorted line-width geometry with loss of image dimension due to increased speed of the reaction. However, when samples are left further in the developer bath well after stripes became clear on the surface, overdeveloping resulted in washing away most of the pattern and causing failure of the lithography process.

After that, samples are rinsed in DI water. Postdevelopment rinse is a required complementary process since removed photoresist residues, or *scums*, may attach

[†]Narrow stripes on the order of a few microns, ensures that the optical wave exhibits zero-order transverse mode behaviour and remains located centrally on the stripe. This can be expressed in terms of active layer thickness for selection of transversal modes in the laser as,

$$d_m = m \frac{\lambda}{2} (n_{R2}^2 - n_{R1}^2)^{-1/2}$$

It means that if the thickness of active layer d becomes smaller than d_m , then the m -th order mode is no longer confined within the laser cavity.

back to the surface and can cause blocking etching in the next step. It is obvious that the resist dissolved in the developer solvent will accumulate as it is used repeatedly. Therefore replacing with new one regularly is necessary to minimize the effect of contamination. Rinsing also prevents resist erosion which may take place in the unexposed areas that absorbed developer solvent.

There exist many other factors that must be considered in a specific optical lithography process. The ones related to laser diode fabrication can be summarized in three separate parts forming a basic lithography system;

- **Alignment and Exposure.** Minimum feature size that can be transferred primarily depends on the quality of imaging system, that is resolution of aligner and on the wavelength of the light. Resolution of the aligner can be expressed as, $R = k\lambda/NA$, where k is around 0.8 and numerical aperture, NA is 0.4 with $\lambda=320$ nm for MJB-3.
- **Mask.** For a reproducible processing mask must be high quality with no defect or dislocations both in glass surface and on the pattern. It is also desired for mask to be highly chemically resistant to glass- and mask-cleaning solutions. Alternatively, it must have high optical transmission in the wavelength range used to expose photoresists.
- **Photoresist and Associated Chemicals.** All the chemicals (including photoresist) must be clean from the dust, dirt and the other particles. For the resist, it is often necessary to filter further as it is done in this process. It must first be chosen to match the resolution of the pattern to be transferred to be able to form fine patterns in low dimensions.

2.5 Etching (Dry)

2.5.1 Etching Techniques

After pattern is defined using resist layer on the front surface, this geometry is transferred onto underlying semiconducting structure by means of etching. Etching process preferably acts in a way to remove any surface material not protected by hardened resist.

Etching can be performed with wet- and dry-etch (gas plasma, ion, or reactive ion etch environment) methods. Wet etching basically uses liquid based (wet) etchants to act. It proceeds at the surface of the GaAs through some ordered chemical reactions: first surface is oxidized, then the oxide (Ga_2O , Ga_2O_3 , As_2O_3 , As_2O_5 , etc.) is dissolved while removing some of the Ga or As atoms from the surface. Chemical etches for GaAs normally consists of an oxidizing agent (commonly H_2O_2) mixed with an acid (like H_2SO_4) or base, as ammonium hydroxide, that reacts with oxides of Ga and As. Examples of etching solutions for some materials can be given as HCl/HNO_3 (3:1) for gold, $\text{HCl}/\text{H}_2\text{O}$ (1:4) for aluminum, diluted HF and H_3PO_4 for SiO_2 and Si_3N_4 . Related to GaAs wet etchants an extensive study has been summarized by Adachi and Oe.⁴¹

Wet etching tends to be an isotropic process[†], etching uniformly in all directions resulting an ordinary hole-like figure. The characteristic wet-etch behaviour of etching laterally at and below the resist layer through substrate is called as *undercutting*. There is no standard by which to measure good or bad undercut: it is just a function of the need of the process and sometimes it can be desired at some levels to get a sloped side-wall. Undercutting can be used as a degree of anisotropy to determine fidelity of pattern transfer. This degree is defined by *aspect ratio* which is basically given as etch-depth to width ratio. In laser diode processing, anisotropic profiles with mirror quality vertical sidewalls which give rise to high aspect ratio values are preferred. Figure: 2.4.a shows the Scanning Electron Microscopy (SEM) picture of a typical isotropic

[†]Wet etching processes along certain crystal planes of crystal materials may produce anisotropic results.³⁸

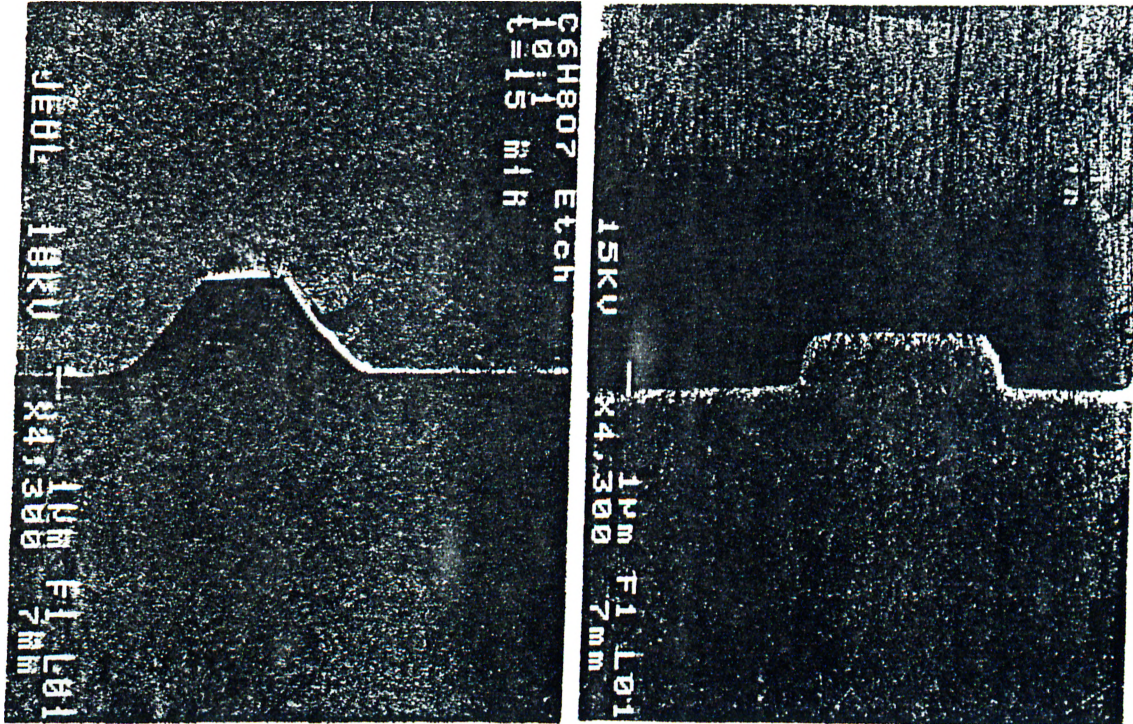


Figure 2.4: Comparison of Wet and Dry etch profiles by SEM.

wet-etching of Hydrogen Peroxide:Citric Acid:DI Water (1 gr:10 gr:10 ml) into n-GaAs (2×10^{18}). Notice the excessive loss in the width of the (initially) $12 \mu\text{m}$ ridge pattern due to undercutting.

Highly anisotropic etching profiles with near-vertical sidewalls can be obtained by dry etching by avoiding the characteristic undercutting problem of wet processes. For comparison, the obtained profile of the same structure after dry etching in CCl_2F_2 plasma (RF power: 54 W, pressure: 0.8 Pa, gas flow: 10 sccm) is also shown in the figure 2.4 where the time was kept constant at 15 min for both processes. Therefore, although rapid etch rates can be performed easily using wet etchants, when directionality and material selectivity is considered dry etch is preferred. The word *selective* is given as a comparison for etches that remove one material faster than another.

Reactive ion etching (RIE) combines other two dry-etch processes; plasma and sputter etching. In plasma etching, wafer is immersed in a gaseous plasma created

by RF excitation in a vacuum system. This plasma contains ions which etch the wafer. Sputter etching uses energetic noble gas ions such as Ar⁺ to bombard the wafer surface and occurs physically. RIE, utilizes both chemical reactions in plasma etching and surface excitation processes of physical sputtering. In reactive ion etching, a gas such as CF₄ is introduced into a reactor with two parallel electrodes across which a radio frequency(RF) voltage is applied. RF is primarily used to obtain higher degrees of ionization and achieve better control over ion energies. The RF voltage causes the reactive gas to break down and form a plasma of ions, radicals and reactive atomic species as a glow discharge in an electric field. This field appears as a steady-state electrostatic force across a thin charge-free region between plasma and the electrodes † called the *dark sheath*. As ions enter this region, they are accelerated towards lower electrode by this built-up electric field and impact on the wafer surface with high energy (reversely, electrons are decelerated). As a result of directed, energetic ion bombardment, reactive neutrals created in plasma enhances etching in the direction perpendicular to the surface.

2.5.2 LE-301 RIE System

Dry etching of submicron geometries is being handled today with RIE (cathode coupling), plasma etching (anode coupling), magnetron RIE and ECR (Electron Cyclotron Resonance) etching systems. In our process, dry etching was performed by using a Leybold-LE 301 parallel plate (planar) reactive ion etching system with a water cooled lower electrode that is powered by an RF source operating at 13.56 MHz. Figure 2.5 shows the descriptive model of RIE system indicating the mechanical rough pump, roots blower and the turbo pump. Grounded top electrode is generally designed to be much larger than the bottom one where the variable distance between can be adjusted up to 6 cm. Process chamber is pumped mainly by TMP-450C Turbo pump to achieve a base

†The strength of this field can be expressed as, $\frac{V_A}{V_C} = \left(\frac{S_C}{S_A}\right)^4$, where V_A , V_C and A_A , A_C are the voltage drops and surface areas of anode(A) and cathode(C) respectively.

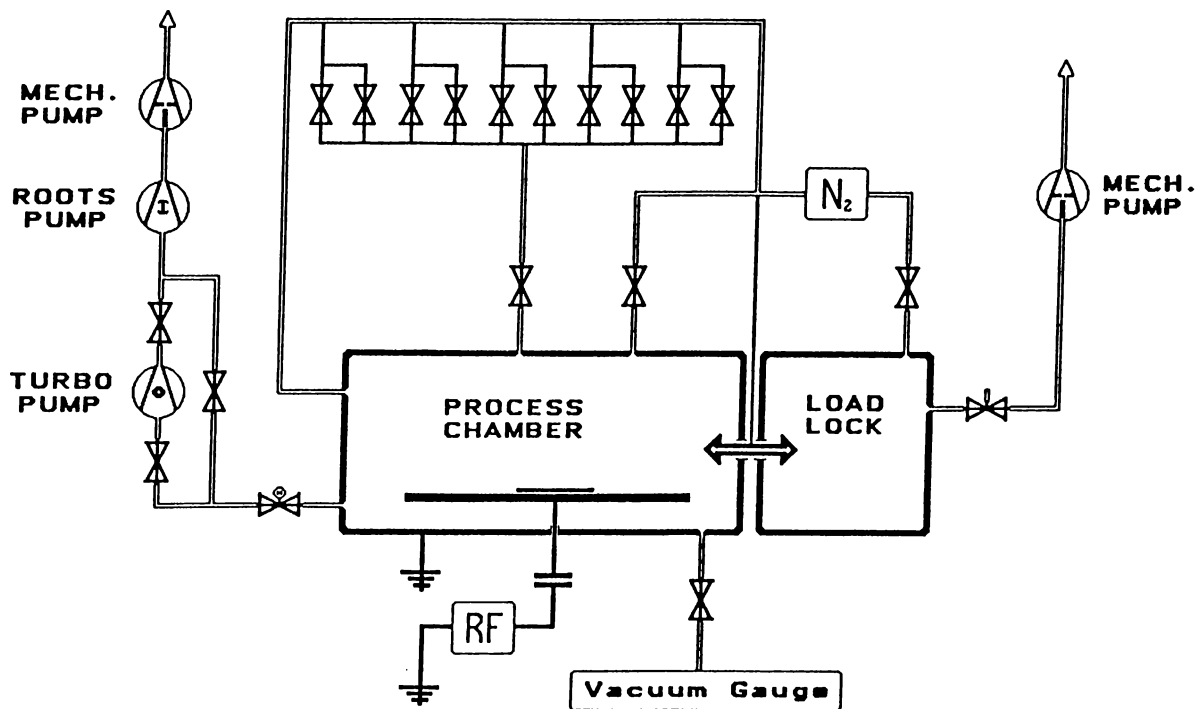


Figure 2.5: Basic schematics of Parallel-Plate LE-301 RIE system.

pressure in the order of 10^{-5} mbar which leads to highly reproducible processing. In operation, the roughing valve is opened first, and the mechanical pump lowers vacuum chamber pressure to an intermediate vacuum level of a few pascals. When this point is reached, turbomolecular pump is operated to achieve high vacuum.

Wafers are inserted into load-lock chamber first, then transferred to the main etch chamber through an arm followed by vacuum pulldown. The gases are then bled into the chamber and rf power is turned on automatically, resulting in a glow discharge that produces plasma. The vacuum level achieved for our process is less than 1 Pa. Process parameters (time, pressure, rf power, gas type and flow, *etc.*) are given to system through a keyboard in the front panel. System, then, fully automatically adjusts the desired parameters to perform etching.

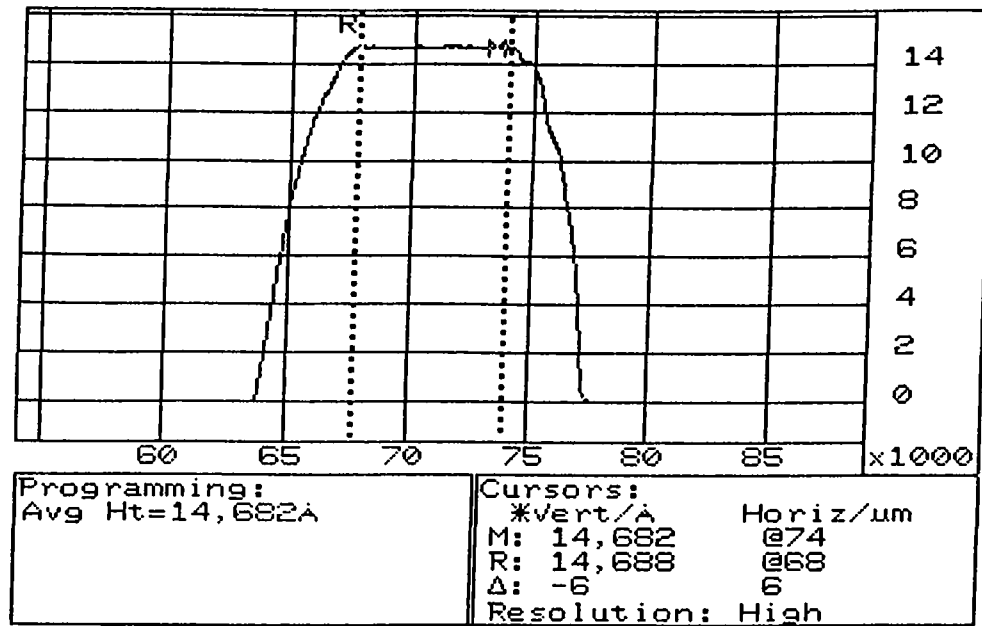
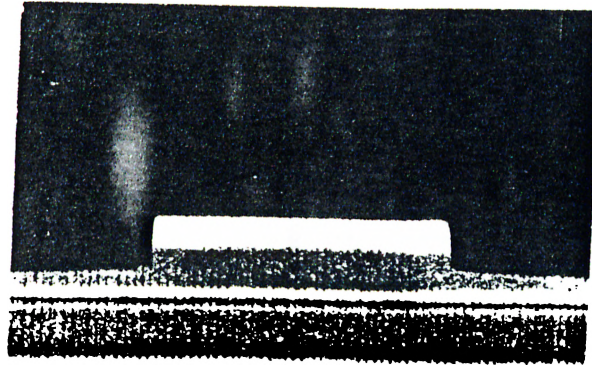


Figure 2.6: Dektak-Profile after etching

2.5.3 Process Description

The ridge waveguide, was then formed by etching away top layers with dry etching using pure Freon-12 (CCl_2F_2) as the reactive gas. Predetermined value of CCl_2F_2 gas flow was 4 sccm. A self bias voltage as high as 300 V was used for these experiments where the electrode spacing held constant at 60 mm. Pressure was kept at 4×10^{-3} mbar ($=0.4$ Pa). Initially RF-power has been set to 46 W but during the process it reached to 54 W value. A multistep etching has been applied while etch depth was detected during etching. Etching was stopped about $0.4 \mu\text{m}$ above the active layer (graded index part of the cladding layer) which results in good lateral-mode confinement for waveguiding purposes. The magnitude of etch depth obtained after the dry etch process was measured by using DekTak-3030ST Surface profilometer as given in figure: 2.6. Accuracy in measuring etch depth is necessary in order to determine exact depth and profile obtained. In this respect, SEM can also be used with its ability to monitor profile uniformities within a precision level down to 50 \AA (Fig. 2.7)

One important point that deserves special attention here is related with over-etching. This problem occurs when etching extends beyond a point at which

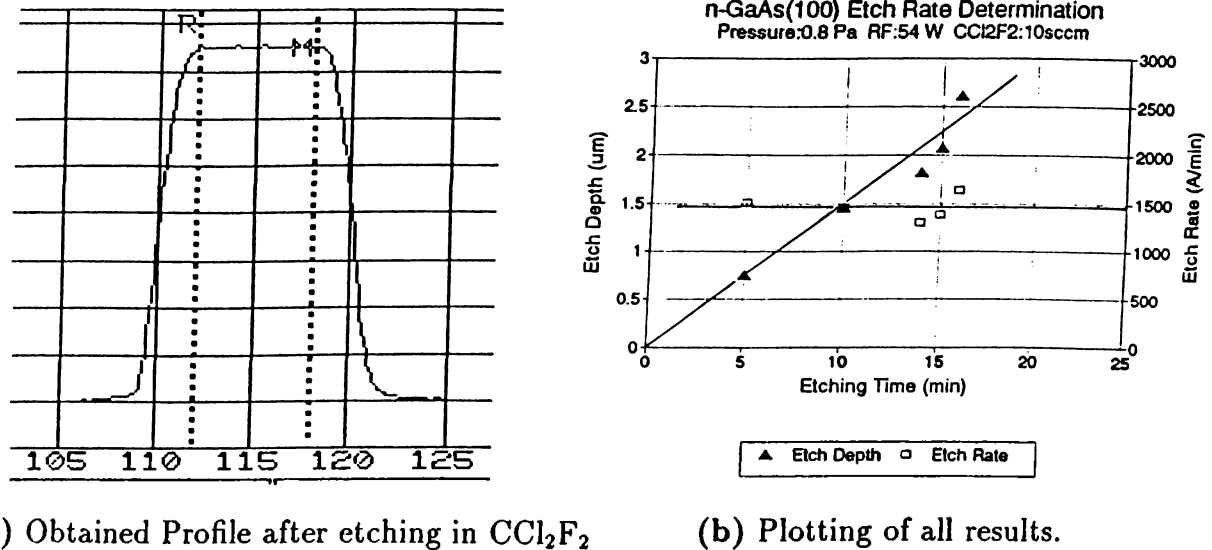


×5000

Figure 2.7: SEM-Profile after etching

structure has been over-etched down to the active layer. Over-etching into the active layer results in introducing traps in the energy gap of the active region, due to bindings with amorphous oxide at the interface. These traps, in turn, cause non-radiative recombinations at the sides of the ridge, giving rise to high leakage currents and leading process to fail. Therefore, it is necessary to adjust parameters carefully to achieve desired depth and observe the level of depth etched with accuracy during etching. In this way, etching was performed so that remained thickness of the cladding layer above the active layer is as small as possible. However, there is a lower limit for this thickness as it must be large enough to cause reflection of the light inside the ridge for lateral optical confinement. Therefore, this level was determined to be $0.4 \mu\text{m}$ for our purposes with considering that it will reduce down to $0.1 \mu\text{m}$ after oxide deposition steps.

The only problem arose in etching with Freon-12 was excessive etching times reaching up to one hour. Although it was a must to spend that much time to etch $0.7 \mu\text{m}$ depth with this recipe, this must be avoided to give less damage to the samples. It was also seen later on that this time interval can be reduced to 15-20 minutes and selectivity down to 1:1 by using Cl_2/BCl_3 plasma as the reactive gas. Etching data related to Cl_2 based plasma is presented in a later section.

(a) Obtained Profile after etching in CCl_2F_2

(b) Plotting of all results.

Figure 2.8: Etch Rate Determination

2.5.4 Etching Analysis

In etching, by varying the process parameters and set-up, profiles with different degrees of anisotropy can be obtained. The issue here is to produce desired geometry by successfully determining the needed recipe for RIE. But, since the result of a specific etching process may vary from system to system, or even, machine to machine, several recipe were tried in order to understand basic etching properties (etch rate, depth, uniformity, *etc.*) of LE-301 RIE system. However, the power of this approach should not be underestimated as our progress in etching optimization for controlling over etch profile, arose from those many trial-and-error experiments. In this respect, etch outputs were studied versus changes in process parameters such as applied bias voltage, pressure, power level, gas percentages in the total flow.

Etch Time versus Etch Depth. General approach to analyse an etching result is to monitor surface profile and to determine etched depth by means of a profilometer or a scanning electron microscopy (SEM). Figure 2.8.a shows such a profile taken by DekTak Profilometer after etching n-type (2×10^{18}) 100-GaAs under 10 sccm CCl_2F_2 flow. For the same recipe, a series of etch depth data was recorded at different etching times to map Freon-12 etching

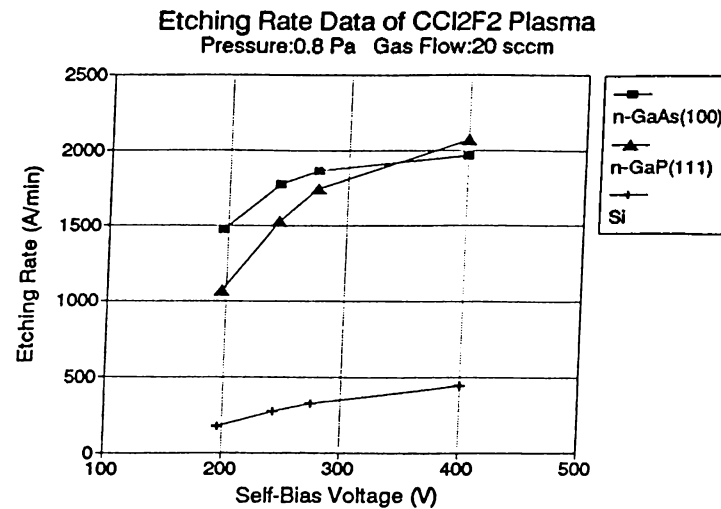


Figure 2.9: Etching of GaAs, GaP and Si under CCl₂F₂ plasma

behaviour.(Fig. 2.8.b) The etch rate can be first calculated simply from the slope of the line as 1500 Å/min. Or, alternately, etch rates for every point can be determined and then an average etch rate value can be taken. This approach is illustrated on the right hand side of the graph where resultant etch rate is slightly less than 1500 Å/min this time. This etch rate value was recorded for future reference, however, it is better to use only in the calculated time interval where the relationship is linear.

Etch Rates of Different Materials. For comparison etch rates of different materials at varying self-bias voltages were studied as shown in figure 2.9. Although increased etch rate values are recorded for increasing voltage, notice that etching of GaAs tends to saturate around 2000 A/min while for GaP it still continuing to increase. However, at this pressure and flow conditions etching of silicon is seen to be acting very slow.

Oxygen Plasma Results. In addition to CCl₂F₂ plasma, oxygen plasma has also been studied. The applied RF-power vs self-bias voltage relationship of both plasmas are given in figure 2.10. As seen, after about 80 watts applied both plasmas respond similarly by creating same bias level. For comparison, different materials have been etched in both O₂ and CCl₂F₂ plasma under same conditions (Pressure: 0.8 Pa, RF Power: 74 W, Gas Flow: 20 sccm, Self-Bias Voltage: 400 V). Obtained etch rate values are tabulated in the next page.

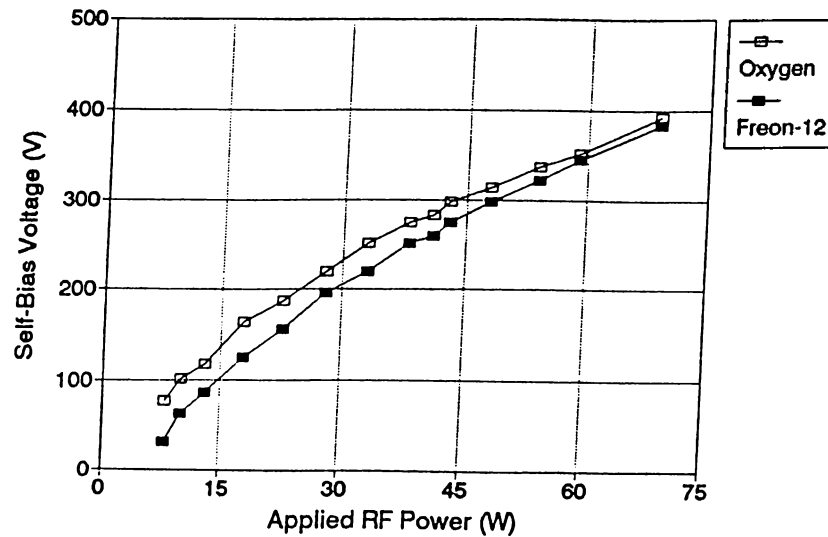


Figure 2.10: Oxygen and Freon-12 Plasma Comparison

Material	CCl_2F_2 Plasma	O_2 Plasma
<i>Si</i>	445	4.8 Å/min
<i>GaP(111)-p</i>	2072	17.3 Å/min
<i>GaAs(100)-n</i>	1968	18.6 Å/min

Although it may seem that etching in oxygen is a time consuming process and not very effective, this low etch rate values are ideal for applying a short post-development treatment of O_2 plasma to remove resist residues on the wafer without deformation.

$\text{Al}_x\text{Ga}_{1-x}\text{As}$ Etching. The etch rate did vary significantly with respect to the Al content in $\text{Al}_x\text{Ga}_{1-x}\text{As}$ layer being etched. We plotted calculated etch rates for x fractions of 0.3, 0.6, 0.7 respectively as shown in figure 2.11. For comparison etching rate of GaAs in the same process parameters (Gas flow: 4 sccm, Pressure: 0.4 Pa, RF Power: 54 W) is also included in the graph. A nonlinear decrease in etch rate with increasing aluminum concentration was observed. These values can also be used in terms of selectivity. This time it can be said that GaAs: $\text{Al}_x\text{Ga}_{1-x}\text{As}$ selectivity increases while etching $\text{Al}_x\text{Ga}_{1-x}\text{As}$ layer with higher aluminum content with this recipe. Respective selectivity values calculated are given on the right hand side of the graph. For example for $x=0.3$, GaAs: $\text{Al}_{0.3}\text{Ga}_{0.7}\text{As}$ selectivity is measured as 2.5:1. This value can be increased

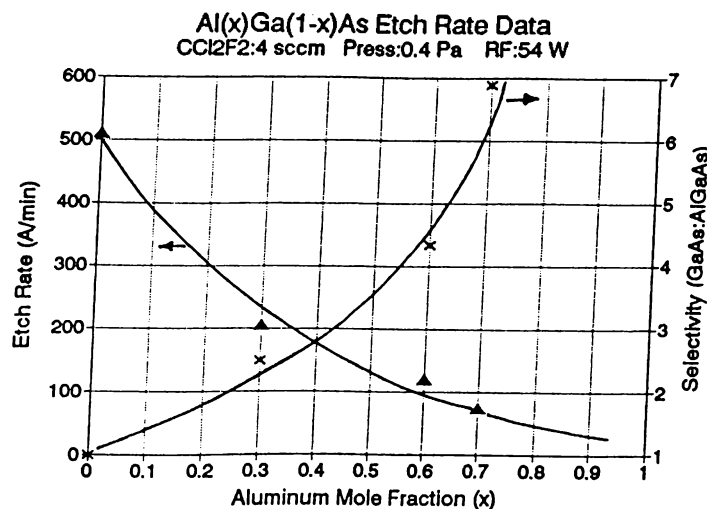


Figure 2.11: Al_xGa_{1-x}As Etch Rate Data.

to a value of 5:1, just twice the initial, if gas flow is increased to 10 sccm and pressure to 0.8 Pa.

Selectivity versus Pressure. In etching, we preferred a process based on CCl₂F₂ (Freon-12) at low gas flow (5 sccm) and pressure conditions so that we can reduce selectivity of AlGaAs over GaAs. The selectivity value of GaAs:AlGaAs can reach to the order of as high as 10,000:1 if operated at moderate pressures and gas flows. For example, at 4 Pa pressure and 12 sccm Freon-12 flow this ratio is found to be around 1000:1 in the process parameters of interest. In this case, etching was nearly stopped when the AlGaAs layer was reached. Further decreasing the pressure down to 0.4 Pa, we could obtain desired values like 5:1 or much better 3:1. However, it required longer pumpdown cycle to achieve that pressure values before etching. It was also seen that selectivity can be decreased by applying high self-bias voltages. However, in the processes where selectivity becomes important, oxygen can be added to the CCl₂F₂ (or any fluorocarbon gas) to increase selectivity.

Etch Rate versus Pressure. At low pressure the RIE of GaAs in CCl₂F₂ shows acceptable anisotropy and etching rate. At high pressure the unsaturated species can be adsorbed at the surface and polymerize by increasing with partial pressure of the unsaturated CCl_xF_y species, thus resulting stop in etch at the end. Low pressure brings the advantage of removing the need for polymer

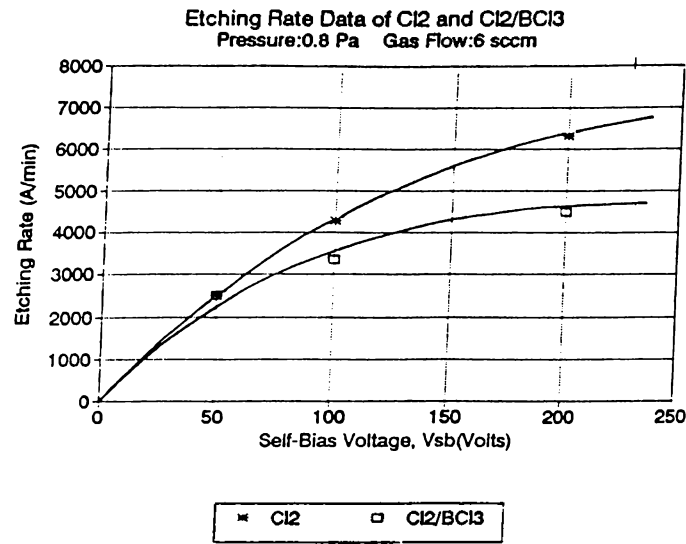


Figure 2.12: Chlorine based plasma results

forming chemistry to provide anisotropy, thus removing a major potential source of contamination. However, at low pressures excess resist erosion starts to take place. Ion bombardment rather than chemical reaction is the main cause of resist loss in this regime. Increasing pressure increases the collision frequency and thereby decreases the ion bombardment energy, resulting in less resist removal and higher selectivity. Knowing this, high-bombardment processes can be applied sometimes on purpose but for a short time (if photoresist selectivity is not so critical) to remove post-development residues existing on the surface.

2.5.5 Cl₂ Based Etching

Chlorinated gas plasmas can also be used in these etching processes. Highly anisotropic GaAs/AlGaAs etch profiles can be achieved using just Cl₂ or a combination like BCl₃/Cl₂ with low pressure conditions. Moreover, formation of non-volatile gallium trifluoride (GaF₃) that may result in using fluorine-based plasmas can also be avoided in this way. In figure 2.12 etching rate data of Cl₂

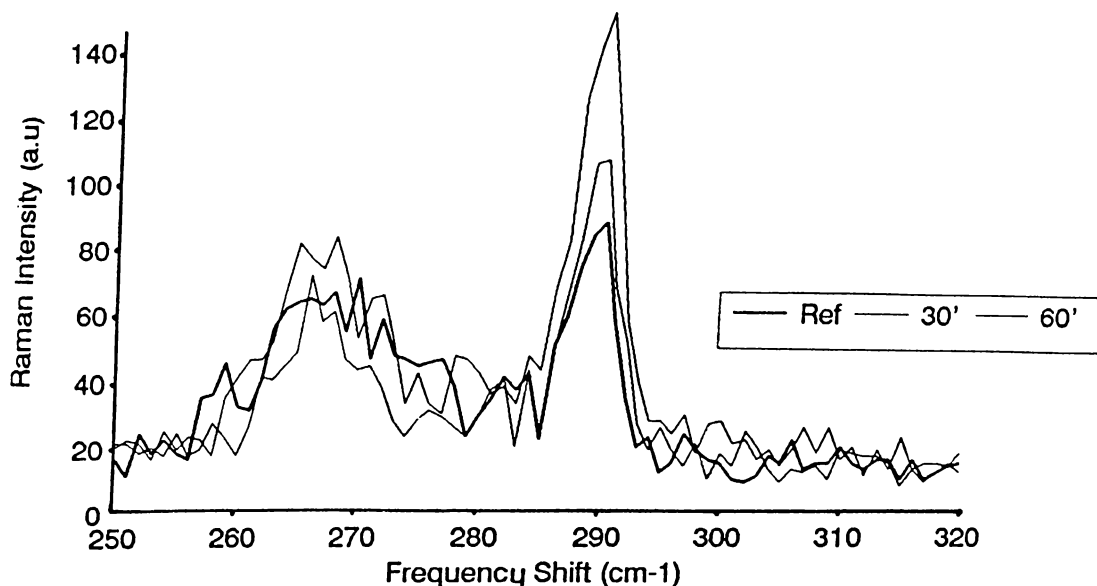


Figure 2.13: Raman Scattering Spectrum of samples

and Cl_2/BCl_3 taken at Ioffe Institute [‡] is reported. Both Cl_2 and Cl_2/BCl_3 etch rates tend to increase exponentially with increasing self-bias voltage. Notice that using Cl_2/BCl_3 as the reactive gas a high rate of 4492 and 6335 Å/min for Cl_2 were obtained at 200 V self-bias voltage whereas for the same process conditions CCl_2F_2 etch rate came out to be as only 2014 Å/min, twice less than the above. However, in spite of their high etching rate nature, these plasmas normally are lack of high selectivity that we have seen in freons.

2.5.6 RIE Induced Damage

RIE induced damage results when applied plasma changes the surface morphology (discontinuity) by causing subsurface damage and creating traps for mobile carriers. A variety of methods such as Photoluminescence, Raman scattering, XPS or SIMS can be applied to study plasma induced damage at or below the surface. In this section use of Raman spectroscopy and Photoluminescence to investigate the strength of damage induced by dry-etching in Freon-12 (CCl_2F_2) plasma is presented.

[‡]A.F.Ioffe Physico-Technical Institute, Russian Academy of Sciences, St.Petersburg, Russia.

In the experiment two n-GaAs samples were exposed to CCl_2F_2 plasma (Pressure: 0.4 Pa, Gas flow: 4 sccm, RF Power: 54 W) at high self-bias voltage for 30 and 60 minutes respectively. Figure 2.13 shows the obtained Raman spectrum of reference (unetched) and two etched samples excited by Ar-ion (5145 Å) laser. Spectra basically contain two peaks, the one which has of high intensity peak is at 290 cm^{-1} is due to longitudinal optical phonons (LO) and originating from the carrier depleted surface region, and the other (268 cm^{-1}) represents coupled plasmon-LO phonon modes (L^-), coming from the undepleted doped-bulk region. In the figure, increased intensity ratios of I_{LO}/I_{L^-} are observed after etching. This ratio which is a measure of depletion layer thickness, d_o is expressed in terms of absorption coefficient of GaAs, α ($= 10^5 \text{ cm}^{-1}$) as,

$$\frac{I_{LO}}{I_{L^-}} = A (\exp[2\alpha d_o] - 1) \quad (2.1)$$

where A is a constant evaluated from equation 2.1 when the depletion depth of unprocessed sample is substituted. If initially, the depletion depth of reference sample is taken as 240 Å^{42} for a doping of 2×10^{18} , then the depletion depths for 30 and 60 min exposition is found from above as 264 and 319 Å respectively. This shows that depletion layer depth increases exponentially with exposition time under high-bias voltages. However, since the depletion increased by only a few tens of angstroms over half an hour etching time, damage induced by dry-etching in Freon-12 plasma can be accepted very low as also indicated by Lishan, *et al.*⁴³ Moreover photoluminescence studies were carried out on the test samples. Figure 2.14 indicates the results in which 60 min etched sample has lowest luminescence efficiency due to nonradiative recombination centers created by surface and subsurface damage, resulting in higher depletion depth. While peak positions remain in the same position, comparison of spectras reveals more clearly the effect of damage.

Earlier cathodoluminescence and Raman studies show that the degree of damage is greater for plasmas with lighter ion mass (H_2) and higher ion energy.⁴⁴ It is also known that damage can be reduced by applying etchings with faster rate or post-annealing.⁴⁵ On the other hand, increased substrate temperature or bias

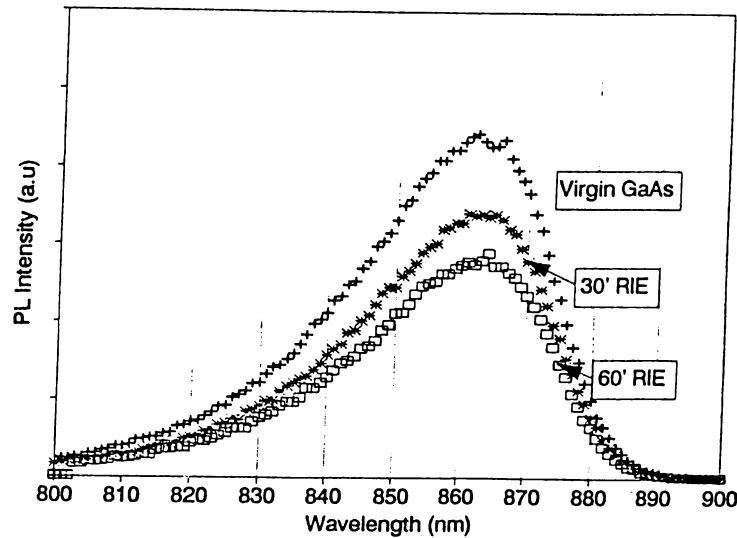


Figure 2.14: Photoluminescence Spectrum of samples etched in Freon-12

voltage tend to increase the effect of damage by increasing the depletion layer depth. In this respect, to reduce etch-induced plasma damage on laser samples, high density plasmas under low pressure conditions was used in this etching step although there had been some difficulty in obtaining sufficiently stable plasma.

2.6 Anodic Oxidation

In this step, it is desired to grow a native oxide layer on the surface by using anodic oxidation method. It is also desired native oxide layer to have acceptable dielectric properties with good structural homogeneity (*i.e.* film must be a uniform) and interface quality so that a rather smooth surface is achieved. The term “Native Oxide” is defined as the residual surface oxide product that is formed when the surface of the GaAs-host crystal is consumed in an oxidizing ambient. For our case the anodically grown amorphous native oxide is expected to be a mixture of Ga_2O_3 and As_2O_3 (possibly the hydrates thereof).

Anodic oxidation solution is prepared in two steps; mixing first Ethylene Glycol ($\text{CH}_2\text{OHCH}_2\text{OH}$):Citric Acid ($\text{C}_6\text{H}_8\text{O}_7$):DI Water with a ratio 200 ml:3 gr:97 ml and then adding ammonia solution until pH level is brought

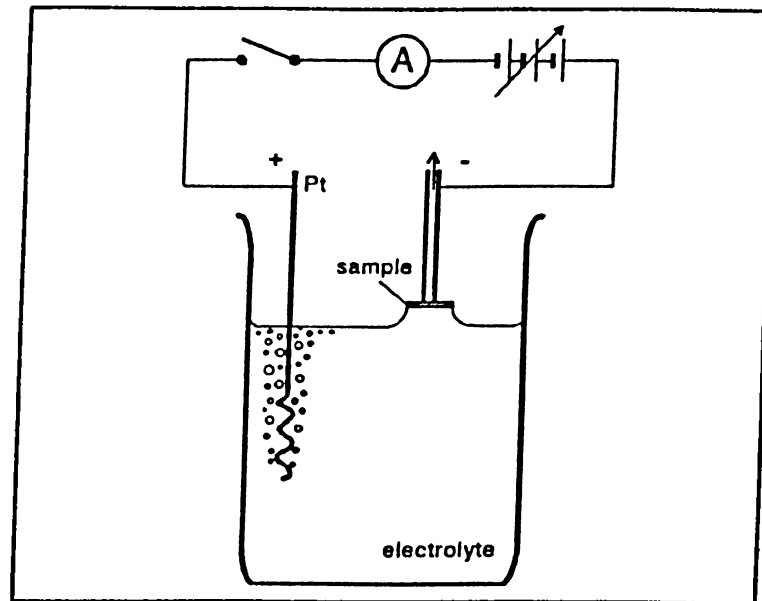


Figure 2.15: Experimental Set-up for Anodic Oxidation

to 6.5. In this oxidation method, as shown in the figure: 2.15 (from ref. 46), a platinum bar is used as cathode. Sample is placed instead of anode with its front face just touching the solution surface. Upon application of forward bias between electrodes, a thin oxide layer starts to grow on the sample surface whose thickness is linearly dependent on the anodization voltage applied. As the thickness of the insulating layer increases, the current going through becomes more restricted and decreases gradually, and after a certain thickness is achieved it completely vanishes. Therefore it can be stated that this oxidation process is of a reaction limited one and native oxide layers with self-limited thickness is grown at the end. For the given electrolyte solution in the constant-voltage mode, average growth rate was obtained as 21 \AA/V for each applied voltage ($V_F \geq 20 \text{ V}$). Therefore, 50 V is applied in order to grow approximately $0.1 \text{ }\mu\text{m}$ thick layer on the surface. Resultant oxide layer gave a deep blue color due to AlGaAs layer at the surface when it is inspected under white light.

One important point about anodic oxidation is that this process is not actually a pure growth but a formation of an oxide layer using some part of GaAs layers underneath due to oxygen ions diffusing into GaAs layers. So, each anodization cycle actually means, removing a well defined amount of GaAs.⁴⁷ Therefore,

growing of around $0.4 \mu\text{m}$ thick oxide layer while it is again $0.3\text{-}0.4 \mu\text{m}$ far from the active layer may result in terminating growth inside this region, and thus giving a complete damage to laser structure.

Related to process, it was observed that obtained growth ratio can be further increased when the sample is sufficiently illuminated by an external light source (*i.e.* lamp).⁴⁸ Also larger area of platinum (possibly a rectangle-shaped plate rather than bar) effects this rate positively and gives more uniform native oxide layers probably due to more directional electric field coming from larger electrode. However formation of bubbles (possibly hydrogen) on the sample surface were seen to be highly effecting the uniformity of oxide layers. In this case, mixing the solution by employing a stirrer inside reduce the number of bubbles.

After the native oxide formation, the resultant surface was smooth and ready for SiO_2 to be grown. It was also shown that reliable native oxide layers is being grown by this method as it didn't break down in subsequent lift-off, metallization and annealing steps.

2.7 Plasma Enhanced Chemical Vapour Deposition (PECVD)

By this deposition step, a thin SiO_2 dielectric layer is formed on the top surface before the contact metallization. This layer both serves as an insulating layer to protect the surface and acts as an integral part of the process for a successful lift-off to be applied.

The PECVD system is basically a computer-driven system in which all the parameters (temperature, pressure, gas flows and ratios, *etc.*) and process sequence can be altered externally. In figure: 2.16, reactive gases (silane and nitrogen) required for SiO_2 formation, are introduced into a chamber in which the sample rests on the bottom electrode (a grounded aluminum plate). An RF signal is applied to the top plate to establish the plasma. Inside the chamber (plasma reactor), gas species are excited by the RF discharge to generate flow discharge

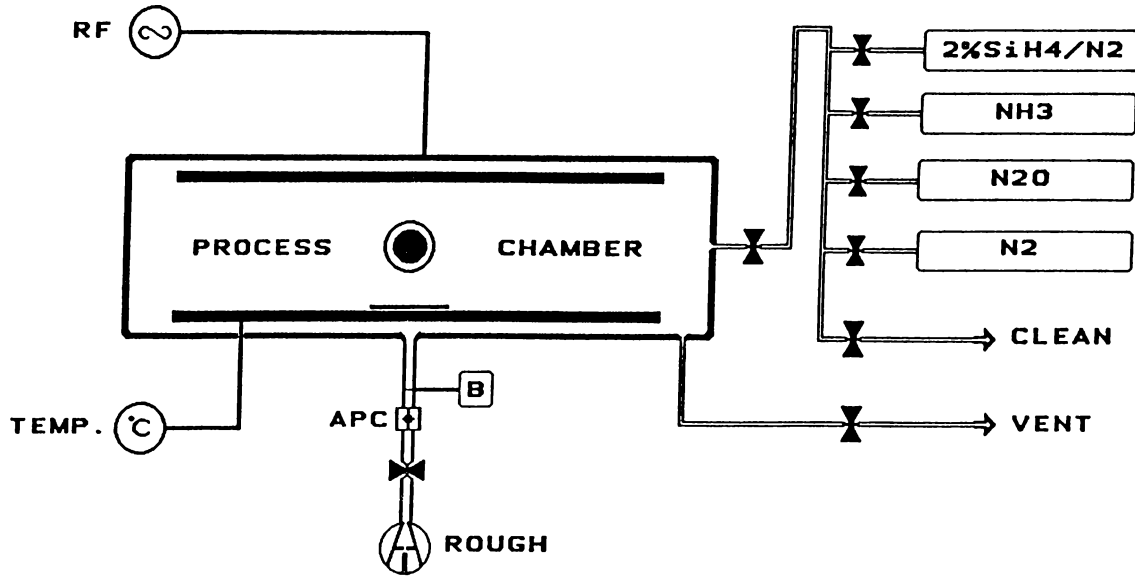
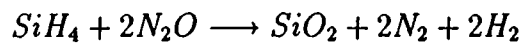


Figure 2.16: PECVD System Layout

and enhance the reaction. Active species present in the plasma enables reactions to take place at around room temperature which would not occur outside the plasma.

In this deposition step, under 300 mTorr chamber pressure plasma is created by introducing 2% SiH₄/N₂ (180 sccm) and N₂O (710 sccm) gases into the chamber at a low temperature of 100 °C. With this recipe 0.1 μm thick uniform SiO₂ insulating layer can be grown at the top of the surface. Chemical reaction takes place inside the chamber and yielding SiO₂ can be written as;



The photoresist is left on the ridges during deposition of 100 nm SiO₂ layer. Actually, this SiO₂ layer coated has a composition of SiO_{1.9}(H) and a dielectric strength of 5 MV/cm.³⁷

Chemical vapor deposition (CVD) processes are done at pressure ranges where movement of molecules is by viscous flow. Among them, plasma enhanced CVD differs from others in that deposition is carried out at low temperatures. Here, the main problem concerning compound semiconductors is to adjust the temperature

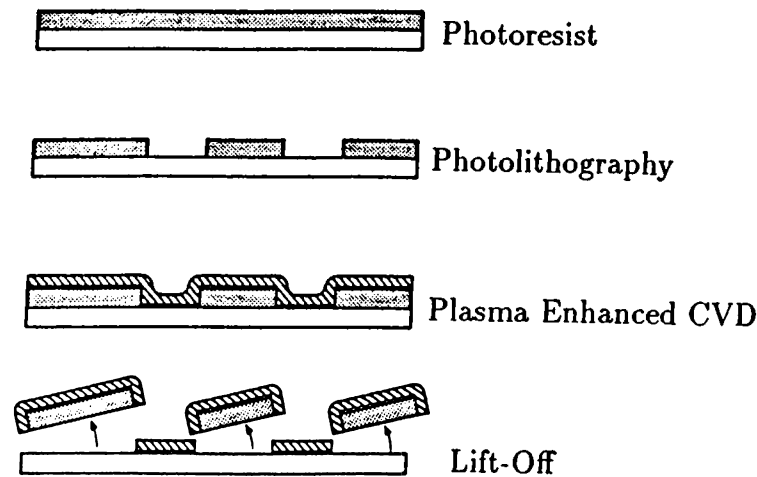


Figure 2.17: Lift-Off Process

to maintain this reaction without causing dissociation of the substrate. Therefore minimization of thermal energy given to the system is necessary as suggested by Plasma Enhanced CVD.

2.8 Lift-Off

In this lift-off step a self-aligning technique is applied to automatically register the contact window over stripe. Previously, SiO_2 was deposited over the entire wafer, landing on top of the ridge-stripe and on the bare areas of wafer surface. Now, application of acetone to remove the photoresist left on the ridges, causes the resist to dissolve, swell and lose adhesion to the wafer. While it is leaving the surface, the insulating layer (SiO_2) on top of the resist is stripped off from the stripe as well. As a result, a window is opened on the stripe which is already required for *p*-type contact-metallization.

In general, acetone is the major solvent used to remove resist either in lift-off or stripping operations. But, application of acetone is typically limited to nonpostbaked resists since residue formation increases as a function of postbake temperature, as reported by Kaplan and Bergin.⁴⁹

A possible problem during lift-off is incomplete removal of photoresist over the stripe. To overcome this, samples are immersed in warm acetone ($\sim 40^\circ\text{C}$)

to increase the penetration. As a result, it was observed that both resist and insulating layer at the top of the ridge are lifted-off more cleanly and easily. Another problem may arise when removed photoresist is re-deposited on somewhere else on wafer surface. Cleaning of sample inside the acetone using a wipe and application of remover were also seen to be suitable.

Most of this lift-off failures arise from the fact that it would be so difficult or impossible to lift off the resist with thicknesses as low as $0.5 \mu\text{m}$. Therefore thicker photoresist layers must be preferred for an easy lift-off. But application of thick resist coating without resolution loss is again hard to get.

2.9 Metallization (*p*-contact)

After defining the waveguide, the metal contact is formed on the top side of the sample for connections. This process based on heating the source material to the point of vaporization in high vacuum atmosphere and then depositing onto sample surface. The chamber pressure on the order of 10^{-6} mbar is achieved in Leybold L560 Box coater before the process started. The samples are initially mounted on a holder with their front surface facing the boat (material holder) below. Materials, such as gold and platinum, are then placed into respective boats and evaporated in order to deposit a thin film covering the surface of the wafer. It is found that poor step coverage occurs in depositing the stripe sidewalls due to directional nature of evaporation. To avoid this problem, the planetary sample holder was oriented to give an angle of about $15\text{--}20^\circ$ in both directions and deposition step was repeated.

Optimized process for *p*-type metallization is Ti/Au (300/2000 Å) Partially, gold is used for the upper metal because its ductile, oxide free nature allows easy bonding.⁵⁰ The reason for our using a 300 Å thick Titanium (which shows good stable thermal properties on GaAs) before Au, was to improve contact quality by providing better adhesion. For *p*-type metallization one can also include coating Pt (around 200 Å) during evaporation which exhibits good resistance to chemical attack. Above 200°C there exists an increase in interdiffusion between GaAs

and Ti, leading to formation of TiO_2 at the surface, thereby degrading the device performance in some amount as reported by Morgan.³⁴ In this respect using Pt is advantageous because its larger barrier height is better at the device's higher operating temperature.

The features desired in a metallization step are contact uniformity, controllable deposition of thin layers, reproducibility and reliability. However, one problem that sometime arose in metallization steps was the easy peeling-off of coated layer from the surface. This may be attributed to thermal expansion mismatch.⁵¹

2.10 Annealing (*p*-contact)

Annealing is made in a high temperature oven (Rapid Thermal Annealer) over a short time period. The main aim for annealing samples after metallization is to improve the ohmic contact quality. Annealing also reduces *p*-coating thickness, and thus series resistance of the final laser is decreased as well.

In the process, samples were annealed at 400 °C under Ar gas atmosphere. For temperature variation, trials of 450 °C for one minute were found to be giving good results as well as our previous application of 400 °C for two minutes.

2.11 Thinning

Back-side of the wafer was then thinned chemically to the desired thickness, typically around 100-110 μm , using a wet etching solution of Hydrogen Peroxide+Ammonia Solution (10:1) for future cleaving and separation. The etching rate of this solution was recorded as approximately 10 $\mu\text{m}/\text{min}$. When the surface obtained is rough, a second thinning of Hydrogen Peroxide+Phosphoric acid+Deionized water (1:1:5) mix application was preferred. Having a slower thinning rate of 7500 $\text{\AA}/\text{min}$, this solution was applied for 4-5 minutes.

There are several advantages coming with thinning to note. First of all, final separating process is easier when dealing with thin samples. This also makes

possible to obtain mirrors with better mirror quality. Obviously, reduction in the wafer thickness brings a reduction in the series resistance of lasers by considerable amount. A thin substrate enables a more efficient thermal conduction path to be followed.

Formation of bubbles when etching highly effected to achieve a uniform etching. For this case, we preferred to use stirrer to avoid nonuniform etching. Stirring while etching is observed to be increasing etch rate up to rates 12-13 $\mu\text{m}/\text{min}$ as it somehow polishes the sample surface as well.

2.12 Metallization (*n*-contact)

In the second metallization step, it is intended to cover the rear surface with a metal layer using evaporation technique. Here, again formation of ohmic contact is desired between the thinned *n*-type substrate and germanium/gold layer to be deposited. The optimized process for *n*-type metallization is to coat layers of Ge/Au/Ni/Au with thickness values of 350/600/250/1500 Å respectively.

One necessary condition for reliable metallization is to keep series (sheet) resistance low by choosing proper coating material. Low resistance minimizes voltage drops across the diode and also decreases propagation delay caused by finite resistance (also capacitance) of the metallic contact layer. In this respect, primarily gold was used for bonding and evaporated with secondary materials such as germanium and nickel to obtain good quality contacts.

Contact quality is crucial to good device performance. A heavily doped substrate enables good quality ohmic contacts to be made to the bottom surface. Thicknesses of coatings are also the parameters required to be optimized. Generally it is preferred to coat Ge/Au to be thicker than 1000 Å, typically 400/2500. This ratio originates from the AuGe eutectic alloy formed by 88% Au and 12% Ge by weight. Therefore after deposition of nickel which acts as a wetting agent for better adhesion of AuGe, an extra overcoat of Au (thicker) is applied.

However, there exists one restriction in using gold; its poor thermal stability. This shows up in GaAs–Au junctions caused by diffusing of gold into the GaAs slightly while Ga diffuses out through the gold and accumulating on the surface. This stoichiometric imbalance, consequently, may result in formation of unwanted interfacial layers (Al_2O_3).

2.13 Annealing (*n*-contact)

The final step in fabrication involves repeating of annealing step for the *n*-side contact as it was done before for the *p*-type. Here, samples were annealed for two minutes in forming gas at 460 °C to achieve a reliable ohmic contact. For this high temperature treatment, it was found out that the samples can also be annealed at 480 °C for one minute. But going up to higher temperatures may result in micro-cracks on the surface.

2.14 Separation of Lasers

To carry out measurements on these fabricated lasers, the wafers were scribed to separate chips having only one stripe per piece with varying cavity lengths between 100 and 750 μm . Great attention must be given in cleaving the finalized lasers as any defect or roughness made on resonator-mirrors seen to be effecting laser performance (especially efficiency) negatively.

The method followed in cleaving starts with discarding areas very close to the sample edges as nonuniform edge shapes occur due to thinning. Then an array of lasers with the same cavity length is cut in the direction perpendicular to stripes. Finally they are separated (diced) to have laser diodes individually. Because of the need to cleave end mirrors by hand for separation, the success to obtain perfect mirrors with this method is limited, but some recent works using microcleaving⁵² or etched facets⁵³ remove the need for bulk cleaving and allow more possibility of having mirror-like side surfaces with optimum accuracy.

In this study, majority of work has been carried out following the given procedure, however repetition and skipping of some steps inevitably occurred because of the problems arised during process run. At this stage, the laser diode fabrication process is completed. There are, however, two further steps to be carried out in a commercial laser diode production. First, chips have to be mounted individually onto a suitable (DIP) package and then very fine bond wires must be used to connect the package electrical terminals to both *p*- and *n*-sides of the laser diode. These steps were not carried out in this work.

Chapter 3

Test Results

3.1 Characterization

In the last phase of the laser diode fabrication process, the electrical and optical characteristics of fabricated lasers were measured so that we can discuss the benefits of our sequential process with given optimization and any performance achieved in this sequential process. In this way a laser performance chart was evaluated for each laser diode in order to qualify that laser for applications and reveal major advantages of MQW lasers such as low threshold current, high efficiency with improved carrier and optical confinement.

This stage started by further grouping fabricated laser diodes with respect to number of quantum wells, varying cavity lengths and stripe widths. Since it is practically impossible to automatically test all the lasers of an array at the same time, test of laser chips were carried out one by one. Therefore a laser holder was used which has an isolated metal plate and a very fine needle-sharp probe where the laser chip is placed in between.

It was then observed that fabricated lasers start to lase between 15-50 mA when driven by a 10 kHz triggered pulse currents of 50-100 ns pulse widths. The reason for driving with pulsed currents is the excessive heating of the laser diodes when continuous currents were used which is highly effective in changing onset value of lasing current.

3.2 Definition of Basic Laser Parameters

Beyond some basic parameters, many laser diode applications require specialized laser characteristics. Here, rather than going into complicated characteristics, giving the basic definitions of common laser diode parameters are preferred.

Parameter	Definition
<i>Threshold Current, I_{th}</i>	Current at which lasing begins.
<i>Forward Voltage, V_F</i>	Voltage drop across diode at specified forward current.
<i>Differential Quantum Efficiency, η_d</i>	Incremental change in optical power output for an incremental change in forward current.
<i>Saturation Current, I_S</i>	Current at which laser output becomes nonlinear.
<i>Peak Wavelength, λ_P</i>	Wavelength at which laser output is max.
<i>Full Width at Half-Max. Intensity, $\Delta\lambda$</i>	Wavelength difference between half half maximum intensity points (FWHM)
<i>Near Field Beam Width, W_x, W_y</i>	Distance between half-intensity points of light exiting laser.
<i>Far Field Beam Width, $\theta_{ }, \theta_{\perp}$</i>	Angular width of beam at half-intensity points parallel/perpendicular to the junction.
<i>Coherence, γ</i>	Attenuation factor of the visibility.
<i>Life-time, T</i>	Determination of number of failures per 1000 device-hours when all operated at constant temperature, current and power.

Note: Laser diode “failure” is defined somewhat arbitrarily as a sudden increase in current of $\geq 20\%$ when it is normally operating.

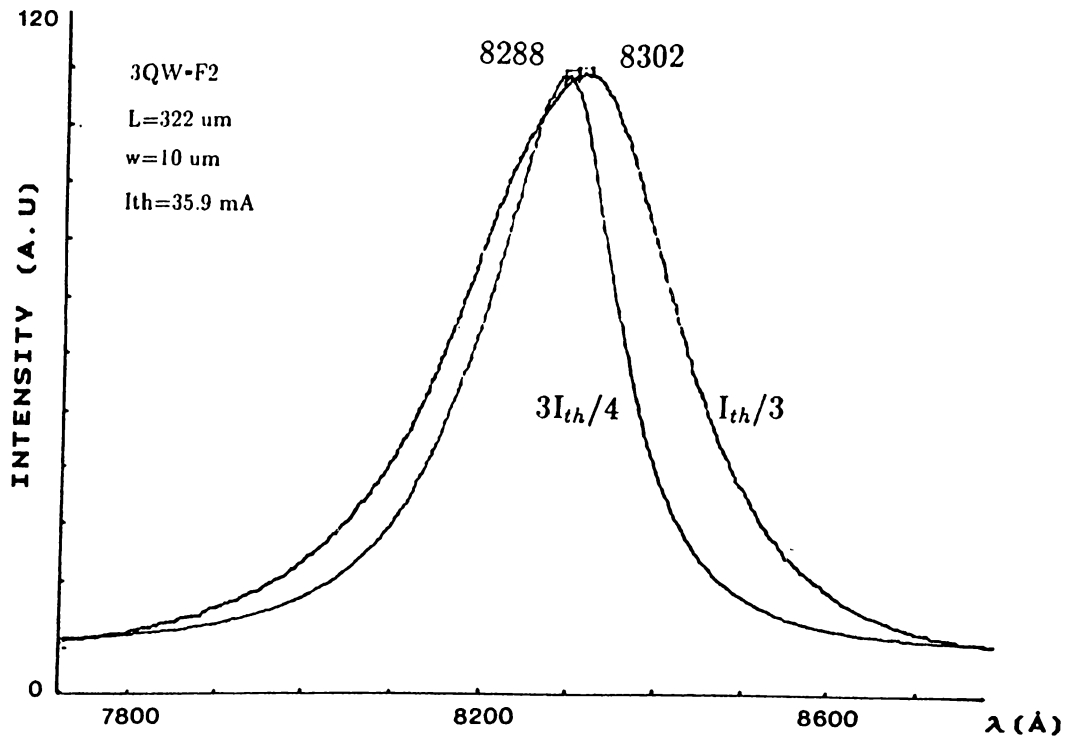


Figure 3.1: Spontaneous Emission Spectra

3.3 Spontaneous Emission Spectra

To understand the basic light emission characteristics of the lasers radiation spectras were measured for driving currents less than the threshold. (Fig. 3.1) At low bias ($I=I_{th}/3$), a relatively broad spectrum was observed which is a result of spontaneous emission. Here radiation is considered to be incoherent. When the applied current was increased to $I_{th}/2$ or to $3I_{th}/4$ the spectra narrowed with the increase in bias. Also a shift from 8302 to 8288 Å in peak wavelength was observed corresponding to higher energies (blue shift).

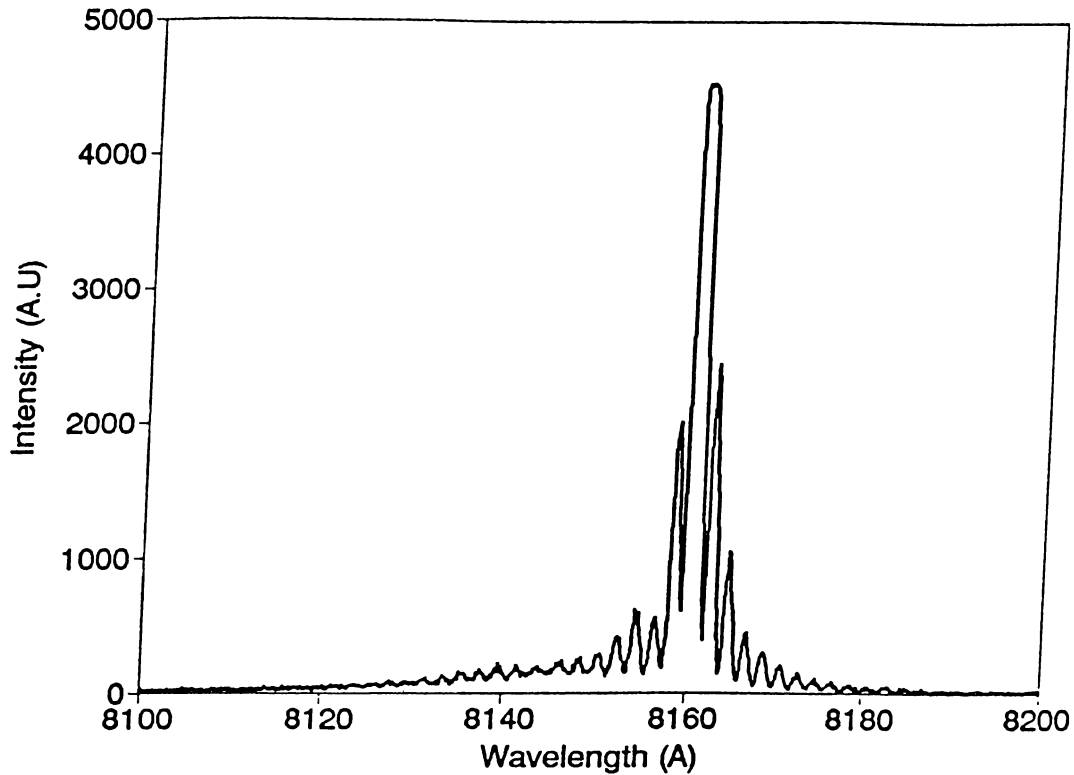


Figure 3.2: Lasing Spectra of 3QW Laser

3.4 Lasing Spectra

A one-meter double monochromator/water cooled GaAs photomultiplier along with standard photon counting techniques was used for lasing spectrum measurements. In figure 3.2, an obtained spectra for the lasing 3QW-K10 laser taken in this way is given. Although this peak is taken for above the threshold, at a current $I=1.5 I_{th}$, a single dominant mode is observed with its very narrow linewidth revealing the monochromatic behaviour of the fabricated lasers. Other small peaks seen nearby the fundamental peak are corresponding to the higher order longitudinal modes with a line separation inversely proportional to the cavity length: $\Delta\lambda = \frac{\lambda^2}{2nL}$.

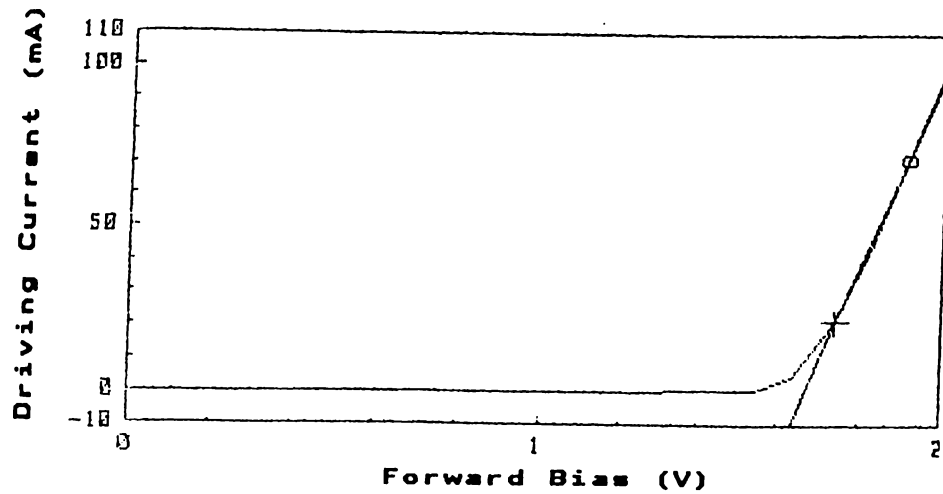


Figure 3.3: I-V Characteristics of 3QW-B4 laser

3.5 Current-Voltage Characteristics

Functional I-V test measurement of lasers were performed in HP-4142 Modular DC Source test set-up where the laser is placed onto a probe station controlled by a computer system. Lasers are driven by constant current source where the current is limited to (initially) 100 mA to avoid excessive heating of lasers which causes to change its electrical response. Overall results showed that lasers start to conduct current after a forward bias of approximately 1.7 volts applied. Thereafter a linear increase is seen in flowing current with applied voltage as shown in figure 3.3. One characteristics which is worthy of specific mention related to this linearity is the series resistance of the laser diode. This value is readily calculated from slope of the curve just beyond the threshold value of voltage. Some of these resistance values along with the turn-on voltages, V_f are tabulated in the below:

Sample:	B4	D10	B6	K8	K6
V_F (Volt)	1.67	1.70	1.66	1.69	1.68
$R_{series}(\Omega)$	3.37	3.16	3.48	3.74	4.36

In this respect we can claim our metallization and thinning steps are successful and quality of ohmic contacts fall within acceptable limits.

3.6 Light-Output vs Current Characteristics

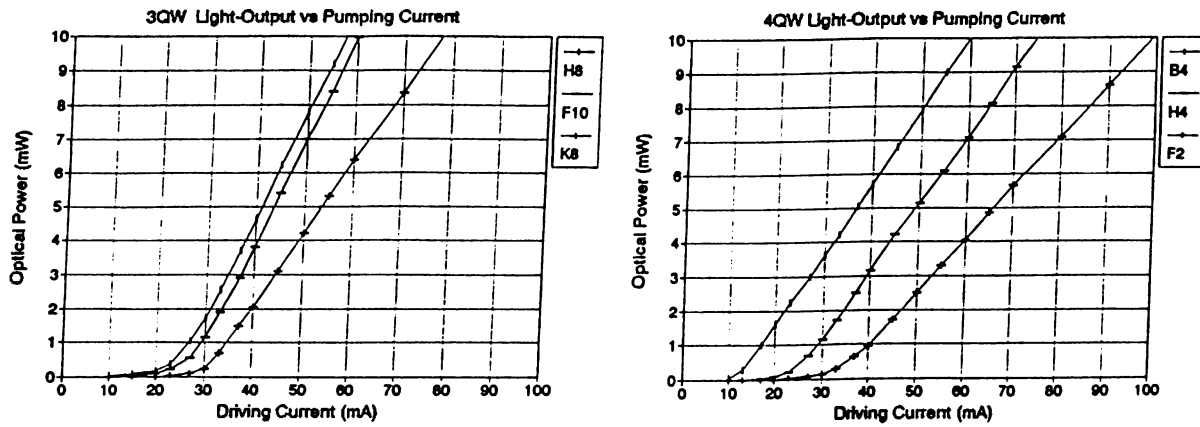


Figure 3.4: I-P_{opt} Characteristics of 3QW and 4QW Lasers

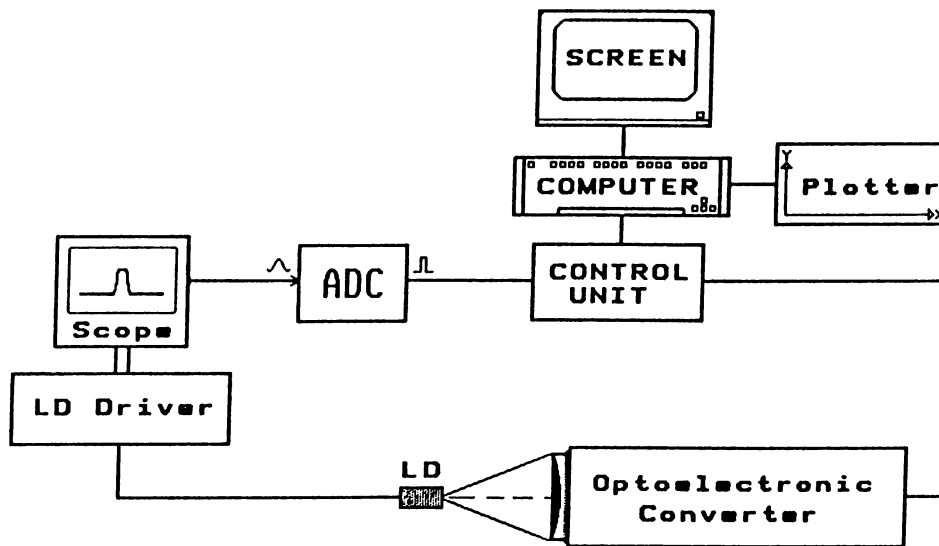


Figure 3.5: Optical Power Output vs Forward Current Measurement System

3.6.1 Threshold Current

Fig. 3.4 shows a few examples of measured pulsed current/light output characteristics of 3QW and 4QW laser diodes using the experimental set-up of figure 3.5. As seen in the I - P_{opt} figures, after a certain critical value of injected current, called as *threshold current*, is achieved, the light output is increasing steadily with increasing drive current. Also notice that within the axis limits, this increment is linear up to drive currents exceeding about five times the threshold value. Separate measurements on lasers with different cavity lengths also showed that they can operate above 10 mW/facet, after which we expect nonlinearities (catastrophic degradations) start to occur.

In the table below, typical threshold currents measured at room temperature for 3QW and 4QW are tabulated with respect to varying cavity lengths (L) and stripe widths (w). In the overall, threshold values changing between 10 and 50 mA were recorded. The lowest one measured was 12.8 mA of 4QW-B4 which is also shown in figure 3.4. Low threshold current lasers seen are of great importance in terms of low power consumption to realise high-reliability lasers in discrete laser fabrication.

3QW				4QW			
Sample:	L (μm)	w (μm)	I_{th} (mA)	Sample:	L (μm)	w (μm)	I_{th} (mA)
D10	140	5	31.4	B4	107	5	12.8
D4	174	10	27.9	K6	134	10	23.3
B8	174	5	29.2	H2	188	10	28.4
H8	181	10	24.7	B2	228	10	31.4
H6	201	10	29.7	B6	255	10	36.1
F10	241	10	27.9	K2	268	10	32.1
H2	241	10	29.7	H8	281	10	37.9

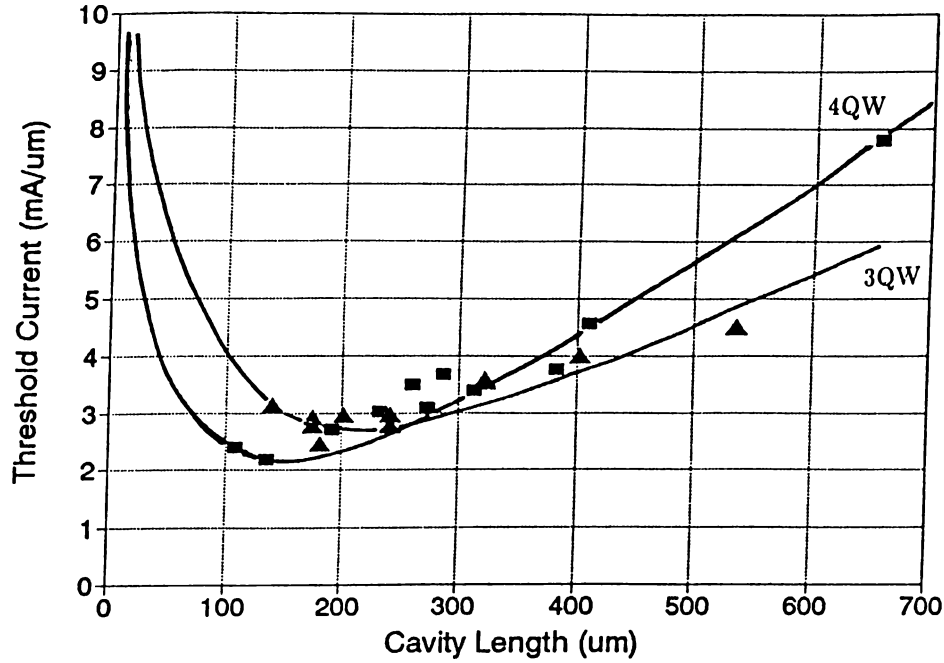


Figure 3.6: Cavity Length dependence of Threshold Current.

Threshold Current versus Cavity Length.

Figure 3.6 shows the dependence of pulsed threshold current, I_{th} (per stripe width) on the varying cavity lengths of three and four quantum well lasers on the same graph. In both, an increase in threshold current is observed with the increase in the cavity length for L is greater than $200 \mu\text{m}$. The increase in I_{th} is due filling of active layer energy bands and finally saturating, and the excessive current causing laser's threshold current to increase. The strong linear dependence of I_{th} on L for long cavity lengths can be expressed by the theoretical formula derived by Mc Ilroy, *et al*,²¹

$$I_{th} = \frac{J_o w}{G_o \Gamma} (\ln(1/R) + \alpha L) \quad (3.1)$$

where it has the form of $I_{th} = a \cdot L + b$ and satisfies with our graphs. For the case of MQW laser with constant cavity length this expression reduces to

$$I_{th} \simeq A n_w \exp(B/n_w) \quad (3.2)$$

with n_w denoting the number of wells and A, B are constants. This expression clearly indicates why we have larger threshold currents in 4QW for long cavity lengths. For every L , above equation can be written in terms of only cavity

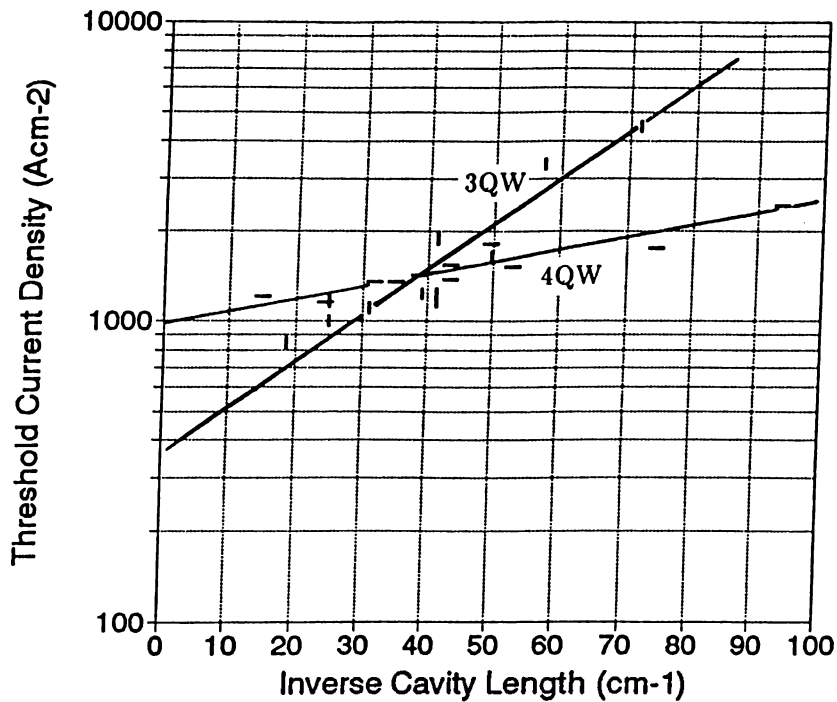


Figure 3.7: Plot of the Threshold Current Density versus Inverse Cavity Length.

length, L as $I_{th} \approx L \exp(\frac{L_{opt}}{L})$ where L_{opt} is the constant optimal cavity length at which I_{th} is minimum. The function defined by this form also describes the shape of the drawn graphs for three and four multiple quantum well lasers, while indicating the perfect matching with the theory. In this respect, the optimum MQW laser with infinite number of wells must show minimum threshold current at zero cavity length. In practice, it is possible when the cavity length is made much smaller than $\ln(1/R)/\alpha$ and for MQW lasers having more than $\alpha/\mathcal{G}_o\Gamma$ number of quantum wells.

Threshold Current Density versus $1/L$.

Another useful way to investigate the threshold behaviour is to draw threshold current density versus inverse cavity length for comparison of MQW lasers with different number of wells. Fig. 3.7 shows a logarithmic plot of calculated threshold current densities of three and four quantum well lasers drawn for reciprocal cavity lengths. As seen in the figure, in low $1/L$ region higher threshold current densities are seen in 4QW samples when compared to 3QW. However, lesser threshold current density is attained at 4QW lasers when inverse cavity length increases.

This can be explained in a way that as cavity length becomes smaller, the mirror loss term, $\frac{1}{L} \ln \frac{1}{R}$ increases and a larger gain is needed to sustain lasing. Therefore, a greater number of wells is required to prevent optical gain from saturating at smaller current densities.

Theoretically this is also expected. Kurobe, *et al* express threshold current density as²²

$$\ln J_{th} = \frac{L_{opt}}{L} + \left(\frac{\alpha}{n_w \Gamma_w g_o} + \ln(n_w J_o / \eta_i) - 1 \right) \quad (3.3)$$

where it has the form of the function $\ln J_{th} = \frac{A}{L} + B$ which corresponds to behaviour of the drawn lines. Notice that the equation decreases more rapidly for large number of wells due to first term ($\sim 1/n_w$) in the paranthesis which satisfies with obtaining lesser threshold current densities in 4QW lasers after $1/L \geq 40 \text{ cm}^{-1}$. The optimum cavity length is generally described as²²

$$L_{opt} = \frac{\ln(R_f R_r)^{1/2}}{n_w \Gamma_w g_o} \quad (3.4)$$

which basically determines the slope of the lines and inversely proportional to number of wells. Here we can deduce why we have larger slope for 3QW lasers. Thus the characteristics of threshold behaviour is fully explained with respective comparisons.

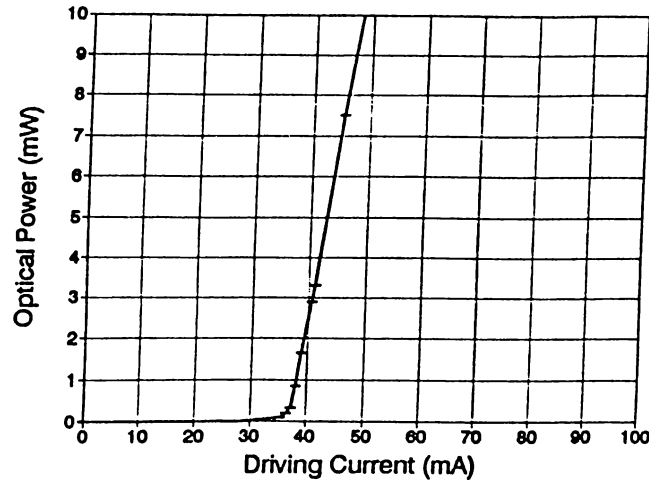


Figure 3.8: Optical Power vs Current Characteristics of Sample-B8

3.6.2 Differential Quantum Efficiency

The pulsed current/light output characteristics obtained for sample B8 from 3QW structure is given in Figure: 3.8. Its threshold current is 29.2 mA, and its differential quantum efficiency is calculated to be around 41.1 %. The light output is increasing steadily with the drive current beyond the threshold well up to 10 mW. If current is further increased above that value it tends to degrade nonlinearly. However in this region there are not any non-linearities, so called *kinks*, seen in characteristics, therefore efficiency remains constant. These kinks especially arise when the applied current is further increased as a result of interaction between injected excessive carriers and optical field.³⁴

3QW			4QW		
Sample:	L (μm)	η_d	Sample:	L (μm)	η_d
B8	174	41.1	h8	281	24.4
F8	241	38.3	H4	281	14.6
D6	322	33.4	F4	308	14.6
K2	402	20.4	D10	308	16.7
D2	536	18.0	F6	375	12.5

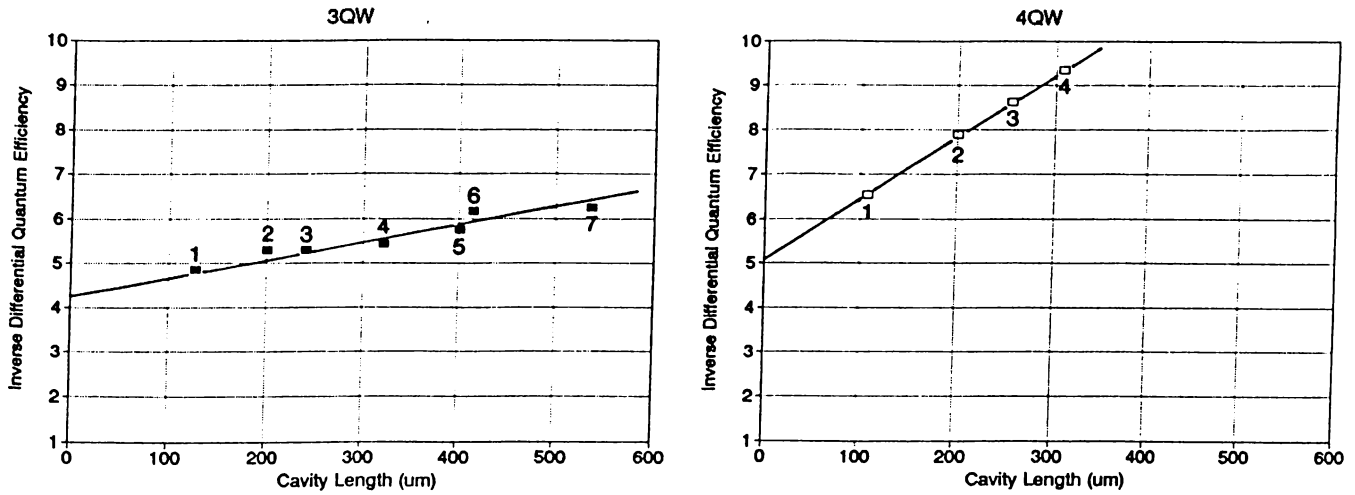


Figure 3.9: Inverse Differential Quantum Efficiency vs Cavity Length

Differential (incremental) quantum efficiency (η_d) values given in table 3.6.2 above were calculated from the slope of the linear portion of I-P curve after the threshold, using the equation $\eta_d = \frac{e \cdot \Delta P}{E_g \Delta I}$. These efficiency values were obtained for a single side mirror and without any anti-reflection coating, therefore can be accepted as a good performance. In general, η_d is expressed as,²⁴

$$\frac{1}{\eta_d} = \frac{1}{\eta_{iN}} \left(1 + \frac{\alpha_{iN} L}{\ln(1/R)} \right) \quad (3.5)$$

where η_{iN} is the nominal internal quantum efficiency and the nominal absorption coefficient, α_{iN} is the loss when when the active layer becomes transparent. The reason for defining a nominal coefficient loss originates from excessive loss in guiding confinement layers in MQW ($\Gamma_{conf} \gg \Gamma_{well}$). Therefore the original expression of equation 3.5 defined for internal efficiency (η_i) is not valid here. In general, nominal internal efficiency is related to differential quantum efficiency by the expression⁵⁴

$$\eta_{iN} = \eta_i \left[1 - (b/a) - (\Gamma_{conf}/\Gamma_{well}) \cdot (c/a) \right] \quad (3.6)$$

where the last expression on the right hand side is normally skipped for double heterostructure lasers. However this effect is important in separate confinement heterostructure MQW lasers confinement in the guiding layers is much larger than in the wells, eventhough the absorption coefficient c is small. Yamamoto *et al*⁵⁴ estimates the constant a , b , c values to be around $\sim 5 \times 10^{-16}$, 10^{-17} , 10^{-18} respectively.

The linear dependence of the reciprocal differential quantum efficiency on the cavity length is indicated in figure 3.9 for some 3QW and 4QW lasers cleaved at various cavity lengths. As seen in the figure η_d decreases with increasing cavity length L . Using the equation 3.5 the $L=0$ intercept of the drawn line in the figure will give η_{iN} . In the graph, for 3QW line η_{iN} has a value of 23.5% and for 4QW it is found as 19.6%. If further reflectivity R is taken as 0.32,²⁵ then the nominal loss α_{iN} can be calculated. This approach is tabulated below for the numbered points in the figure 3.9,

	α_1	α_2	α_3	α_4	α_5	α_6	α_7
3QW	12.76	13.89	11.58	9.86	9.98	12.42	10.00
4QW	29.98	30.83	30.84	30.79			

These loss values are coincident with the theory of Yamamoto mentioned above. He combines nominal internal absorption coefficient with the optical confinement in the guiding layers (Γ_{conf}) and in the wells (Γ_{well}) in the equation

$$\alpha_{iN} = \alpha_o + \Gamma_{well}(\alpha_{wo} + b n_o) + \Gamma_{conf}(\alpha_{co} + c n_o) \quad (3.7)$$

which indicates that as Γ_{well} increases it is expected that nominal absorption coefficient increases as well. Since Γ_{well} for 4QW is higher than that of 3QW (more specifically we assume $3\Gamma_{4QW} = 4\Gamma_{3QW}$) α_{iN} for 4QW will be higher as it was verified with experiment.

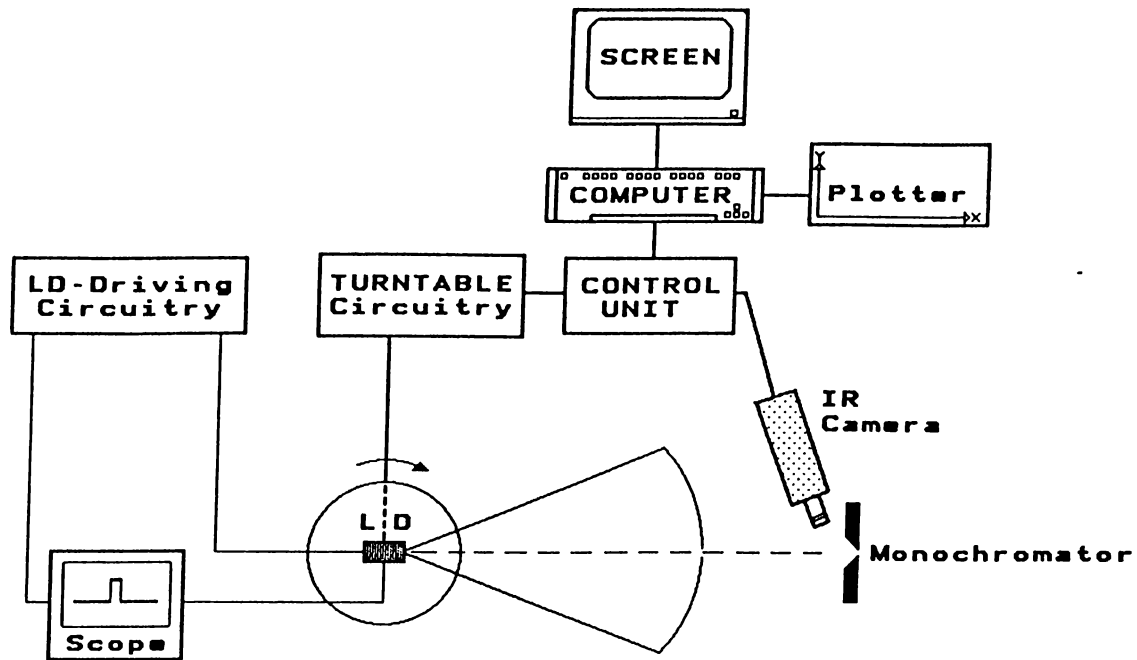


Figure 3.10: Experimental Set-up for Far-Field Measurements

3.7 Field Distributions

3.7.1 Far Field Pattern

Far field radiation characteristics was measured by using the arrangement given in figure 3.10. The laser diode is fixed to to the turntable which is rotated by a mechanical gear-box circuitry. The radiation intensity at each position is monitored using an infrared camera focused onto monochromator input that is illuminated by laser light. The driving current of the laser diode was adjusted externally for various injection levels in order to map far field behaviour above threshold value.

Measured far field patterns of 3QW lasers given in figure 3.11 indicates fundamental mode is stabilized inside the ridge waveguide effectively. The lateral far-field intensity profile given in this figure is taken at driving current value of 52, 58, 65, 79, 92 mA respectively. This far field has a lateral full-width half-maximum (FWHM) spread of about 10 degrees. The slight misorientation of the

peak value at zero degrees originates from the lack of alignment of the rotary turn-table system and must be ignored.

Although the measured far field pattern of Figure 3.11 is single-lobed showing first-order mode is excited at that level, one obtained lateral far-field pattern for 4QW (Fig.3.12) reveals the fact that light is concentrated within one to three longitudinal modes around 820 nm for this laser. However, it is seen that pattern symmetry is still conserved both below and well beyond the threshold current. Alternatively, very fine and confined field pattern was observed for the same laser in the transverse direction without any other higher order modes.

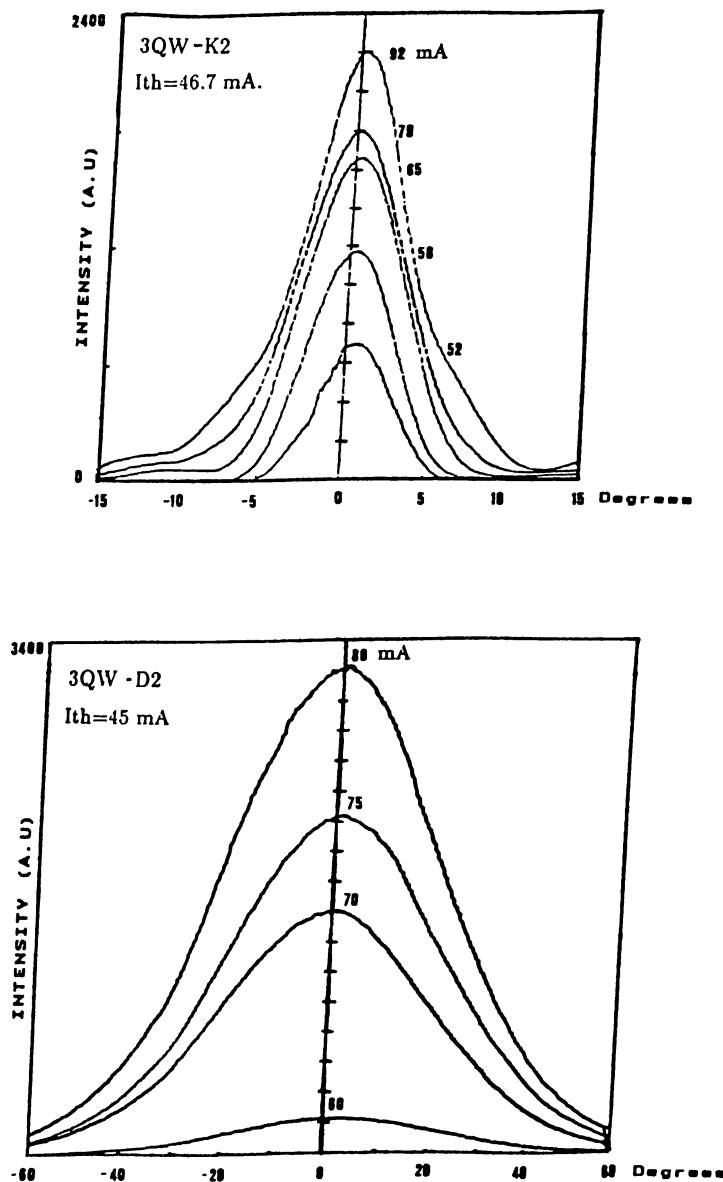


Figure 3.11: Lateral and Transversal Far Field Pattern of 3QW Lasers

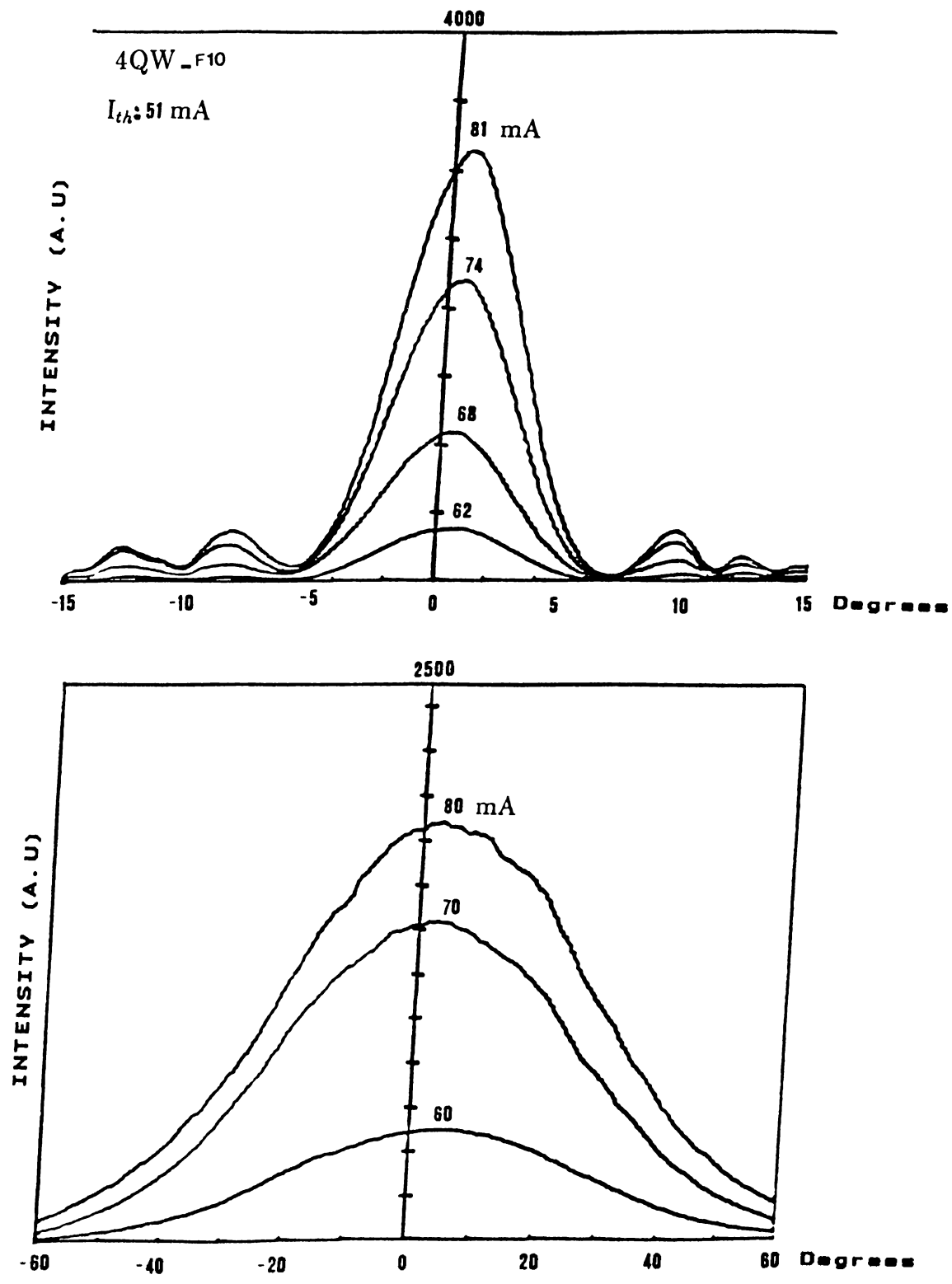


Figure 3.12: Lateral and Transversal Far Field Pattern of 4QW Lasers

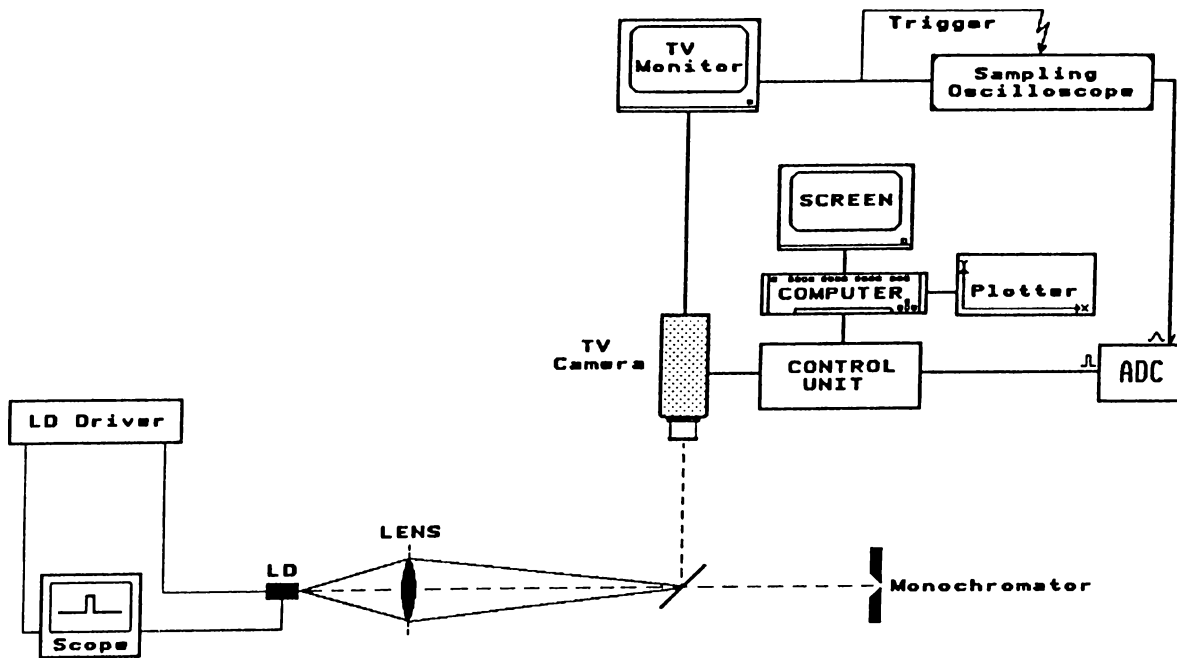


Figure 3.13: Near-Field Radiation Pattern Measurement System

3.7.2 Near Field Pattern

As shown in figure 3.13, the near-field pattern was observed by focusing a lens on the light emitting surface of the laser diode. Then the radiation pattern was enlarged several hundred times and projected onto a screen by means of a vidicon TV camera. The signals obtained on TV monitor were further sampled and digitized to send plotter through a host-computer.

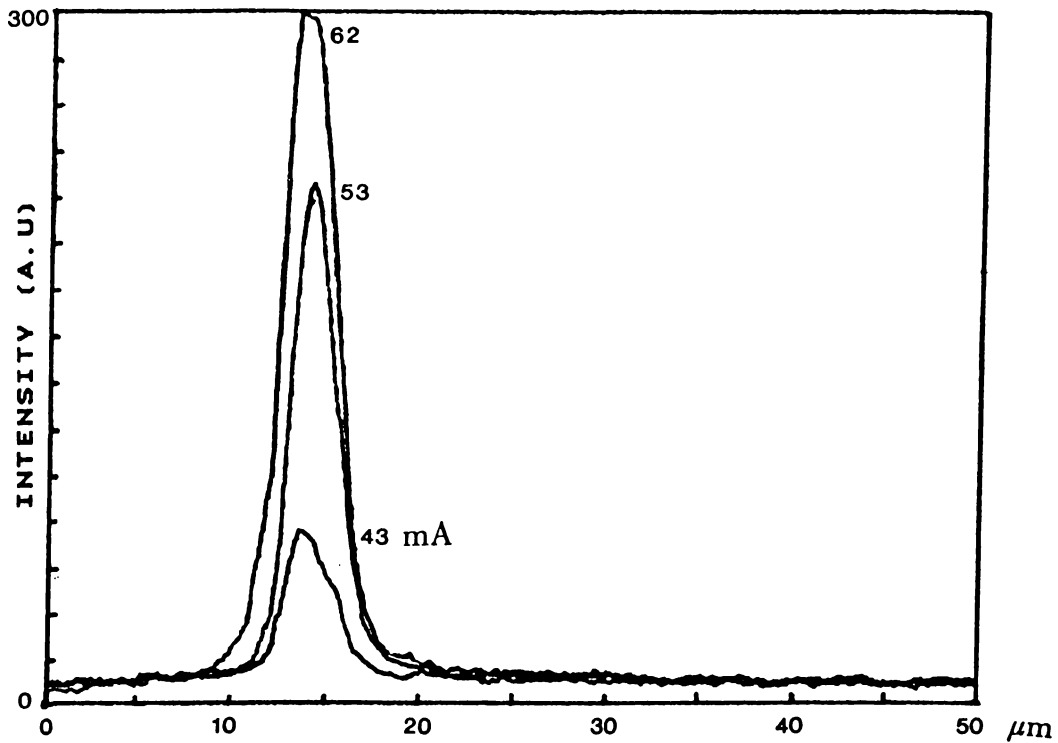


Figure 3.14: Lateral Near Field Pattern of 4QW-K10 Laser

Figure 3.14 shows the near field pattern of a four quantum well laser (K10) taken parallel to the active layer. Its threshold current was determined to be 46.4 mA from I-P measurements and three curves are drawn on the same graph corresponding different injection levels below and above the threshold. At below threshold, 43 mA, light is seen to be conserved in the resonator. Optical confinement shows improvement above threshold indicating the fundamental mode narrows with higher intensity at 53 and 62 mA. Sharpness of the patterns taken for such a wide measurement range also verifies the good quality of side mirrors.

Chapter 4

Conclusions

It is important to note that the statements and observations reported in the preceding sections are drawn, in large part, from three successful process sessions and among varying bodies of data. On the one hand laser diodes with different quantum wells have been fabricated and tested yielding good high-efficiency characteristics and low threshold currents. On the other, some test results of lasers belongs to same structure and process run were found to be showing slight different forms which were attributed to factors that are beyond our control (*i.e.* structure nonlinearities, defects and contamination ...)

In conclusion,

- Ridge-waveguide MQW injection diode lasers were fabricated and studied. Lasers with a threshold current as low as 12.8 mA (for a 107 μm -4QW) and differential quantum efficiency as high as 41% for a single side (174 μm -3QW) were obtained.
- Ridge-waveguide laser diode fabrication through single photolithography step has been shown to be possible.
- RIE using the selective Freon-12 plasma as the reactant gas, was applied for mesa structure formation and etch characteristics has been determined on different materials.

- Structural defects induced by RIE in GaAs/AlGaAs were studied and low defect dry-etching of Freon-12 plasma has been realized.
- Lift-off of low temperature PECVD grown SiO₂ was applied for self-aligned isolated ridge-type laser structure formation.
- Threshold current/density versus varying cavity lengths characteristics has been studied for different MQW lasers.
- Efficiency and loss characteristics of MQW lasers have been determined.
- Optical field distributions near and far from the laser mirror were analyzed both parallel and perpendicular to the active layer.

Appendix

Properties of GaAs and $\text{Al}_x\text{Ga}_{1-x}\text{As}$

Property [†]	GaAs	$\text{Al}_x\text{Ga}_{1-x}\text{As}$
Lattice Constant (Å)	5.65325	$5.6533 + 0.0078x$
Crystal Density (g/cm ³)	5.3174	$5.36 - 1.6x$
Melting Point (°C)	1238	$1238 - 58x + 560x^2$
Static Dielectric Constant	13.18	$13.18 - 3.12x$
Electron Affinity (eV)	4.07	$4.07 - 1.1x$ ($0 \leq x \leq 0.45$) $3.64 - 0.14x$ ($0.45 < x \leq 1.0$)
Band Gap Energy (eV)	1.424	$1.424 + 1.247x$ ($0 \leq x \leq 0.45$) $1.9 + 0.125x + 0.143x^2$ ($0.45 < x \leq 1$)
Refractive Index (n_R)	3.59	$3.59 - 0.71x + 0.091x^2$
Lattice Thermal Resistivity (cmK/W)	2.27	$2.27 + 28.83x - 30x^2$
Density-of-states electron mass:		
Γ valley	0.067	$0.067 + 0.083x$
X valley	0.85	$0.85 - 0.14x$
L valley	0.56	$0.56 + 0.1x$

[†]Values are taken at room temperature as discussed by Adachi⁵⁶ and Blakemore.⁵⁵

Bibliography

- [1] J.K.Butler, *Semiconductor Injection Lasers*.
IEEE PRESS Selected Reprint Series, New York: Wiley, 1980.
- [2] R.N.Hall, G.E.Fenner, J.D.Kingsley, T.J.Soltys, R.O.Carlson, *Coherent Light Emission from GaAs junctions*. Phys.Rev.Lett. **9**, N9, p366, 1962.
- [3] N.Holonyak, S.F.Bevacqua, *Coherent(visible) Light Emission from GaAs_{1-x}P_x Junctions*. Appl.Phys.Lett. **1**, N4, p82, 1962.
- [4] M.I.Nathan, W.P.Dumke, G.Burns, F.H.Dill, G.Lasher,
Stimulated Emission of Radiation from GaAs p-n Junctions.
App.Phys.Lett. **1**, N3, p62, 1962.
- [5] R.H.Rediker, T.M.Quist, R.J.Keyes, W.E.Krag, B.Lax, A.L.McWhorter,
Semiconductor Maser of GaAs. Appl.Phys.Lett. **1**, N4, p91, 1962.
- [6] Zh.I.Alferov, V.M.Andreev, E.L.Portnoi, M.K.Trukan,
AlAs/GaAs Heterojunction Injection Lasers with a Low Room-Temperature Threshold. Sov.Phys.Semicond. **3**, p1107, 1970.
- [7] J.J.Hsieh, J.A.Rossi, J.P.Donnely, Appl.Phys.Lett. **28**, p709, 1976.
- [8] R.D.Dupuis, P.D.Dapkus, *Very Low Threshold Ga_{1-x}Al_xAs-GaAs Double-Heterostructure Lasers Grown by Metalorganic Chemical Vapor Deposition*. Appl.Phys.Lett. **32**, N8, p473, 1978.
- [9] M.S.Tyagi, *Introduction to Semiconductor Materials and Devices*.
New York: Wiley, 1991.

- [10] E.S.Yang, *Microelectronic Devices*. New York: McGraw-Hill, 1988.
- [11] H.Kressel and J.K.Butler, *Semiconductor Lasers and Heterojunction LED's*. New York: Academic Press, 1977.
- [12] R.D.Burnham, W.Streifer, L.Paoli, N.Holonyak, *Electron.Lett.* **18**, p1095, 1982.
- [13] R.Chin, N.Holonyak, K.Hess, R.D.Dupuis, P.D.Dapkus, *Temperature dependence of threshold current for quantum-well $Al_xGa_{1-x}As-GaAs$ heterostructure laser diodes*. *Appl.Phys.Lett.* **36**, p19, 1980.
- [14] H.Iwamura, T.Saku, T.Ishibashi, K.Otsuka, *Dynamic Behaviour of a GaAs-AlGaAs MQW Laser Diode*. *Electron.Lett.* **19**, p180, 1983.
- [15] W.T.Tsang, *A Graded-Index Waveguide Separate-Confinement Laser with Very Low Threshold and a Narrow Gaussian Beam* **39**, N2, p134, 1981.
- [16] N.Holonyak, M.Kolbas, R.D.Dupuis, P.D.Dapkus, *Quantum-Well Heterostructure Lasers*. *J.Quantum Electron.* **16**, p170, 1980.
- [17] Y.Arakawa, A.Yariv, *Theory of Gain, Modulation Response, and Spectral Linewidth in AlGaAs Quantum Well Lasers*. *J.Quantum Electron.* **21**, N10, p1666, 1985.
- [18] W.T.Tsang, *Extremely Low Threshold (AlGa)As Modified Multi Quantum Well Heterostructure Lasers grown by Molecular-Beam Epitaxy*. *Appl.Phys.Lett.* **39**, N10, p786, 1981.
- [19] Hiroshi Okamoto, *Optical properties of superlattice and MQW laser diode*. *J.Vac.Sci.Technol.* **B3**, N2, p687, 1985.
- [20] T.Ikegami, *Reflectivity of Mode at Facet and Oscillation Mode in Double-Heterostructure Injection Lasers*. *IEEE J.Quan.Electron.* **8**, p470, 1972.

- [21] P.Mc Ilroy, A.Kurobe, Y.Uematsu,
Analysis and Application of Theoretical Gain Curves to the Design of Multi-Quantum-Well Lasers. J.Quant.Electron. **21**, N12, p1958 ,1985.
- [22] A.Kurobe, *et al.*, *Effects of Well Number, Cavity Length, and Facet Reflectivity on the Reduction of Threshold Current of GaAs/AlGaAs Multiquantum Well Lasers.* J.Quantum Electron. **24**, N4, p635, 1988.
- [23] H.C.Casey and M.B.Panish,
Heterostructure Lasers. Academic Press: New York, 1978.
- [24] B.Mroziewicz, M.Bugajski, W.Nakwaski, *Physics of Semiconductor Lasers.* North-Holland: Amsterdam, 1991.
- [25] W.T.Tsang, *Extremely Low Threshold (AlGa)As Graded-Index Waveguide Separate-Confinement Heterostructure Lasers Grown by Molecular Beam Epitaxy.* **40**, p217, 1982.
- [26] G.H.B.Thompson, *Physics of Semiconductor Laser Devices.* Wiley: New York, 1980.
- [27] W.X.Zou, T.Bowen, K.Law, D.B.Young, J.L.Merz,
1.0 mA-Threshold Uncoated Lasers by Impurity-Induced Disorder. Photon.Tecchnol.Lett. **5**, p591, 1993.
- [28] H.Narui, S.Hirata, Y.Mori, J.Quant.Electron. **28**, p4, 1992.
- [29] T.R.Chen, A.Yariv, J.E.Ungar, B.Zhao, Y.H.Zhuang, *Ultralow threshold multiquantum well InGaAs lasers.* Appl.Phys.Lett. **60**, p1782, 1992.
- [30] E.Kapon, S.Simhony, J.P.Harbison, L.T.Florez, P.Worland,
Threshold current reduction in patterned quantum well semiconductor lasers grown by molecular beam epitaxy. Appl.Phys.Lett. **56**, p1825, 1990.
- [31] R.Dingle, C.Gossard, W.Wiegman,
Direct Observation of Superlattice Formation in a Semiconductor Heterostructure. Phys.Rev.Lett. **34**, N21, p1327, 1975.

- [32] C.Weisbuch, R.Dingle, A.C.Gossard, W.Wiegmann,
Solid State Commun., **38**, p709, 1981.
- [33] *Book of SEMI Standards*. Semiconductor Equipment and Materials Institute, Inc., Mountain View, CA 94043
- [34] M.J.Howes, D.V.Morgan,
GaAs Materials, Devices and Circuits Wiley: New York, 1986.
- [35] A.C.Adams, B.R.Pruniaux, *GaAs Surface Film Evaluation by Ellipsometry and its Effect on Schottky Barriers*. *J.Electrochem.Soc.* **120**, p408, 1973.
- [36] Garner, *et al.*, *Effect of GaAs or Ga_xAl_{1-x}As Oxide Composition on Schottky-Barrier Behavior*. *J.Appl.Phys.* **50**, p3376, 1979.
- [37] R.C.Jaeger, *Modular Series on Solid State Devices*. Volume:V
Addison-Wesley: Massachusetts, 1988.
- [38] R.Williams, *Modern GaAs Processing Methods*. Artech House: London, 1990.
- [39] W.S.DeForest, *Photoresist: Materials and Processes*.
McGraw-Hill: New York, 1975.
- [40] D.J.Elliott, *Integrated Circuit Fabrication Technology*.
McGraw-Hill: New York, 1989.
- [41] S.Adachi, K.Oe, *J.Electrochem.Soc.*, **130**, p2427, 1983.
- [42] F.N.Timofeev, *Reactive ion etching for fabrication of integrated optic and optoelectronic elements*. AIP-Workshop on the Physics of Semiconductor Lasers, June, 1991.
- [43] D.G.Lishan, H.F.Wong, D.L.Green, E.L.Hu, J.L.Merz,
Dry etch induced damage in GaAs investigated using Raman scattering spectroscopy. *J.Vac.Sci.Technol.B* **7**, N7, p3, 1989.

- [44] H.F.Wong, D.L.Green, T.Y.Liu, J.L.Merz, *Investigation of reactive ion etching induced damage in GaAs-AlGaAs quantum well structures*. J.Vac.Sci.Technol.B. **6**, N6, p1906, 1988.
- [45] E.L.Hu, *Current Trends and Issues for Low Damage Dry Etching of Optoelectronic Devices*. SPIE Proceedings Reprint, Volume 1361, 1991.
- [46] J.S.Wellen, F.Karouta, C.Schemmann, E.Smalbrugge, F.Kaufmann, *Manufacturing and Characterization of GaAs/AlGaAs Multiple Quantum Well Ridge Waveguide Lasers*. EUT Reports (92-E-265), 1992.
- [47] B.Schwartz, CRC. Critical Rev. Solid State Sci. **5**, p609, 1975.
- [48] H.Yamamoto, S.Arimoto, H.Hasegawa, H.Ohno, *Anodic Oxidation of a-Si:H Films*. Electron.Lett. **19**, N1, p6, 1983.
- [49] L.H.Kaplan and B.K.Bergin, *Residues from Wet Processing of Positive Resists*. J.Electrochem.Soc. **127**, N2, p386, 1980.
- [50] D.V.Morgan, K.Board, *Semiconductor Microtechnology* 2nd Edition. Chicester, Wiley: UK, 1990.
- [51] D.V.Morgan M.J.Howes, S.D.Mukherjee, J.G.Smith, P.Brook, J.Vac.Sci.Technol. **16**, p138, 1979.
- [52] A.Yariv, H.Blauvelt, S.Margalit, D.Fekete, *AlGaAs Lasers with Micro-Cleaved Mirrors Suitable for Monolithic Integration*. Appl.Phys.Lett. **40**, p289, 1982.
- [53] J.C.Bouley, J.Rion, N.Bouadma, *Short-cavity AlGaAs Laser by Wet Chemical Etching*. Electronics Lett. **18**, p879, 1982.
- [54] K.Tanaka, K.Wakao, T.Yamamoto, H.Nobuhara, T.Fujii, *Dependence of Differential Quantum Efficiency on the Confinement Structure in InGaAs/InGaAsP Strained-Layer Multiple Quantum-Well Lasers*. Photon.Tech.Lett. **5**, N6, p602, 1993.

- [55] J.S.Blakemore, *J.Appl.Phys.* **53**, pR123, 1982.
- [56] S.Adachi, *GaAs, AlAs, and $Al_xGa_{1-x}As$: Material parameters for use in research and device applications.* *J.Appl.Phys.* **58**, N3, R1–R29, 1985.